



Quantum scattering in one-dimensional periodic structures: A Green's function approach solved through continued fractions

L. R. N. Oliveira  and M. G. E. da Luz *Departamento de Física, Universidade Federal do Paraná, Curitiba-PR, 81531-980, Brazil*

(Received 21 February 2024; revised 27 June 2024; accepted 17 July 2024; published 2 August 2024)

In the present contribution, we discuss quantum scattering in 1D periodic finite lattices of N localized potentials by means of an exact Green's function approach. By considering continued fraction techniques, we solve the resulting recurrence relations, thus being able to derive the full structure reflections R_N and transmission T_N amplitudes in a closed analytic form. The framework allows for dealing with extremely large arrays, in some examples for N up to 10^{10} cells (or building blocks). For so great N 's, in practice the protocol can unveil most of the basic features of the energy band structures of the corresponding infinite systems, demanding relatively little computational effort. We further investigate general scattering properties of distinct lattices, e.g., when their cells are spatially asymmetric or composed by two or more elementary shapes, each shape commonly modeled in the literature in terms of Dirac's delta, rectangular, trapezoidal, and triangular barriers. As concrete applications, we address the problem of parameter optimization of heterostructures used to build solar cells and the identification of some transmission resonance modes, relevant in the study of band-pass transmission in superlattices.

DOI: [10.1103/PhysRevB.110.054303](https://doi.org/10.1103/PhysRevB.110.054303)

I. INTRODUCTION

Scattering is a fundamental process in nature, consequently a powerful tool for its understanding [1]. This is particularly true when one seeks to unveil and explore the general properties of periodic lattices (finite or infinite) through wave scattering [2,3]. Actually, the number of applications made possible through the development of scattering methods in two and three dimensions is countless (for a glimpse see, e.g., Refs. [1,4–7]). Yet, many phenomena can be described simply in terms of one spatial dimension (1D), so that 1D scattering theory is likewise very useful to study a great diversity of systems [8,9].

For instance, superlattices (e.g., made of graphene [10] or of arbitrary semiconductor materials [11]), nanowires (e.g., made of a 10 nm wide and 500 nm long silicon piece [12]) and multijunctions (as solar cell devices formed by the juxtaposition of thin arrays of distinct semiconductors [13]) are commonly represented as a succession of a large number of equally spaced rectangular barriers and can be generally treated as a 1D quantum multiple scattering problem [14]. Shorter 1D systems can be handled in the same way. As an example we cite topological edge modes in 1D photonic structures [15], arising in the interface between two different finite crystals and investigated in terms of open systems scattering. Quantum dots can also be analyzed through scattering approaches, like in metallic single-walled carbon nanotubes [16].

We also should remark that propagation and diffraction of acoustic waves in lattices may be viewed as a multiple scattering problem. Indeed, Ref. [17] has studied trapped modes and resonance transmission in a plate with notches by means of a 1D quantum scattering model, obtaining good agreement with laser Doppler vibrometry. Further, experiments have confirmed 1D scattering predictions for the vibrational

behavior of a structure of Helmholtz resonators connected to a tube [18].

A traditional and important protocol to investigate scattering in 1D periodic finite systems [19–21] is the transfer matrix (TM) method; for two nice reviews see, e.g., Refs. [22,23]. But as usually the case for any interactive calculation scheme, some few limitations may arise in the TM usual formulation [24,25]. This includes issues related to numerical stability [26] and long computational times [27]. Moreover, for super periodic potentials—i.e., structures displaying multiple periodicity, a common feature of superlattices—the TM can display certain computational drawbacks related to size [28]. This has motivated improvements in the procedure (for instance, those in Refs. [24,25,28–31]). However, even with such advancements, the examination of lattices containing, say, more than 10^3 scatters (barriers and/or wells), continues to pose great challenges.

Surely, other mathematical techniques are also available [8,32–35]. Among them, continued fractions (CF) solution methods are rather powerful. In 3D, CF has been used to address the Lippmann-Schwinger equation [36–38], allowing to analyze the scattering of electrons and positrons by atoms [39], electrons by linear molecules [40], and low-energy electrons by hydrogen molecules [41]. In 1D, by discretizing the Schrödinger equation one can compute the associated transmission and reflection coefficients through CF-like recurrence relations [42,43]. Moreover, by expanding the Laplace transform of time-correlation functions in terms of CF, we can calculate generalized susceptibilities and transport coefficients [44], in addition to relaxation memory functions [45], in lattice structures. Beyond wave phenomena, CF has found valuable usages to explain infinite resistor network puzzles [46], determine the dielectric response of collisionless plasma [47] and to resolve the renormalization group equations for

a ferromagnetic Gaussian measure on \mathbb{Z}_+ , yielding its time decay rate [48].

A key common characteristic of the previous systems is to be able to cast the equations governing the quantities of interest in terms of recurrence relations. This allows to solve these equations via CF-like constructions—details in the next section. Complying with this prerequisite, it has been demonstrated [49–53] that scattering in 1D lattices composed by a series of N nonoverlapping localized (or more formally, compact support) potentials V is particularly suitable to a Green's function G approach. Indeed, by adding a new V to a structure already with $N - 1$ short-range barriers and/or wells V 's, the resulting scattering amplitudes can be obtained from a recurrence relation derived directly from G .

In this work, we suppose a basic localized potential, which we call a building block (BB), and whose reflection and transmission coefficients are somehow known, either from analytical or numerical methods. Then, for an equally spaced 1D array of N BBs, we show how to solve the recurrence relations—derived from a Green's function treatment—for the resulting full R_N and T_N through CF techniques. The obtained exact expressions are computationally very simple to implement. This enables one to calculate extremely large networks, e.g., for $N = 10^6$ and even $N = 10^{10}$, with a minimal numerical cost. Relevant to mention that as already observed in the literature [24,25,27,28], such huge N 's would be very hard to deal with employing other protocols as the TM.

As a general development of our method, we examine various scenarios and lattice properties, such as energy band structures and the implications (for transport) of spatially asymmetric and/or composite BBs, employing as basic shapes the Dirac delta, rectangular, trapezoidal and triangular barriers, all having closed expressions for the individual scattering amplitudes. Along the way, we also discuss distinct applications that our suggested framework might have in real-world situations. In particular, we illustrate how to apply our approach to optimize the spatial parameters of heterostructures considered in the fabrication of solar cells and how to characterize Fabry-Pérot (FP) transmission resonance modes in certain superlattices (intended for use as band-pass filters).

The paper is organized as the following. In Sec. II, we briefly review how to obtain the exact recurrence relations for the scattering coefficients of a collection of N compact support potentials through a Green's function method. In Sec. III, we show how to write these relations in terms of CF. This leads to exact formulas for the associated T_N and R_N . We also discuss the limit of $N \rightarrow \infty$. In Sec. IV, we present theoretical applications for our scheme, addressing general scattering properties of lattices with various types of BBs. In Sec. V, we analyze two concrete problems, optimization of heterostructures for solar cells and the identification of FP resonance modes in superlattices. Finally, in Sec. VI, we draw our final remarks and conclusion.

II. EXACT GREEN'S FUNCTION AND RECURRENCE RELATIONS FOR REFLECTION AND TRANSMISSION COEFFICIENTS

Assume N nonoverlapping compact support potentials V_1, V_2, \dots, V_N in 1D, illustrated in Fig. 1(a). We denote by r_n

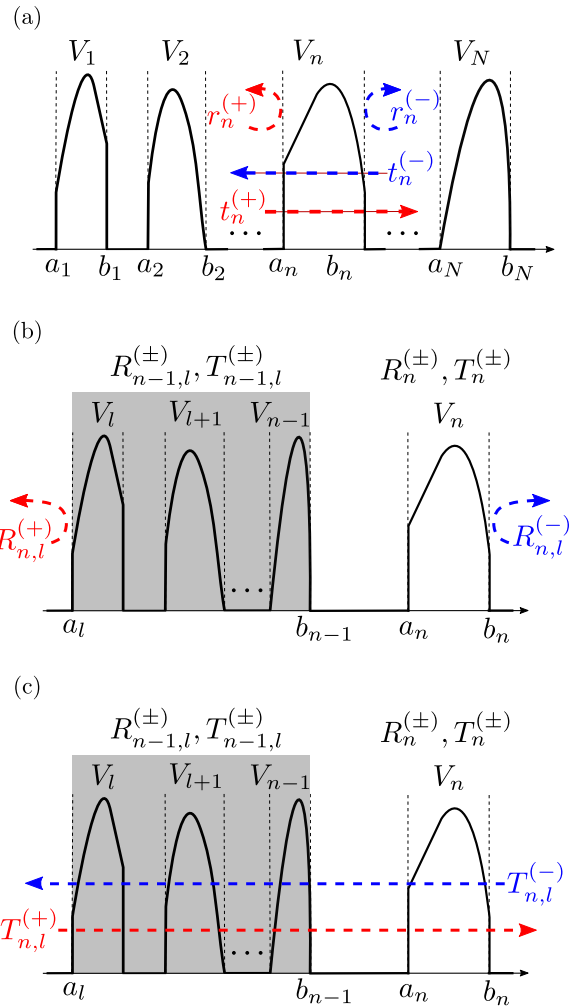


FIG. 1. (a) A collection of N nonoverlapping compact support (localized) potentials V_n ($n = 1, \dots, N$). In detail the schematics of the usual reflection $r_n^{(\pm)}$ and transmission $t_n^{(\pm)}$ quantum amplitudes for a single V_n in the case of a plane wave incoming from the left (+) or from the right (-). [(b) and (c)] A part of the original system, composed by the potentials $V_l, V_{l+1}, \dots, V_{n-1}$ —forming the block (shaded region) $V_{n-1,l}$, of coefficients $R_{n-1,l}^{(\pm)}$ and $T_{n-1,l}^{(\pm)}$ —and by V_n , of coefficients $R_n^{(\pm)}$ and $T_n^{(\pm)}$. It is also pictorially illustrated (arrows) the resulting reflection $R_{n,l}^{(\pm)}$ and $T_{n,l}^{(\pm)}$ coefficients. For the relations of R with r and of T with t see the main text.

and t_n the usual quantum mechanics reflection and transmission amplitudes of V_n . Suppose now that $V_n(x)$ [as highlighted in Fig. 1(a)] is not null only for $a_n < x < b_n$. Associated to a plane wave + (-), of wave number k and incoming from $x < a_n$ ($x > b_n$), we write $r_n^{(\pm)}(k) = \exp[\pm 2ikc_n^{(\mp)}]R_n^{(\pm)}(k)$ and $t_n^{(\pm)}(k) = \exp[-ik(b_n - a_n)]T_n^{(\pm)}(k)$, with $c_n^{(+)} = b_n$ and $c_n^{(-)} = a_n$. Thus the coefficients R_n and T_n are essentially the scattering amplitudes r_n and t_n up to phases related to the V_n ending points [49]. Obviously, to compute probabilities we can use both expressions once $|r_n|^2 = |R_n|^2$ and $|t_n|^2 = |T_n|^2$. For problems with the time-reversal symmetry—the situation in all our examples in the next sections—we additionally have $T^{(\pm)} = T$.

For the system of Fig. 1(a), the correct Green's function $G(x_f, x_i; k)$, with x_f, x_i outside any potential V_n and

$E = \hbar^2 k^2 / (2m)$, can be cast as an expression akin to a semi-classical formula (for sake of simplicity in the derivations, we suppose a same mass m everywhere, the case of distinct effective masses in the different V_n 's will be addressed in Sec. V). Indeed, for s.p. standing for ‘‘scattering path,’’ the exact G reads [49]

$$G(x_f, x_i; k) = \frac{m}{i\hbar^2 k} \sum_{\text{s.p.}} W_{\text{s.p.}} \exp \left[\frac{i}{\hbar} S_{\text{s.p.}}(x_f, x_i; k) \right]. \quad (1)$$

Each s.p. represents a multiple scattering trajectory, where the particle leaves from x_i , suffers multiple transmissions and reflections by the localized potentials and finally gets to x_f . For a given s.p., $S_{\text{s.p.}} = k L_{\text{s.p.}}(x_f, x_i)$ with $L_{\text{s.p.}}(x_f, x_i)$ the path total length considering only the propagation outside the V_n 's regions. By its turn, $W_{\text{s.p.}}(k)$ is the product of the successive coefficients $T_{n'}(k)$'s and $R_{n''}(k)$'s ‘‘gained’’ along the way, i.e., corresponding to the instances of transmissions through the potentials $V_{n'}$ and reflections from the potentials $V_{n''}$. The sum in Eq. (1) is performed over all the infinite many possible s.p..

It might seem that the above sum, yielding G , is too cumbersome to be carried on. Fortunately, this is not the case. Through some hierarchical procedures (see, e.g., Refs. [49,53]) the s.p.'s can be identified and then organized as geometric series. In this way, Eq. (1) can be summed up exactly in a closed analytic form. Following this type of idea, one can further derive recurrence relations [50–52] allowing to obtain the Green's function for N in terms of that for $N - 1$ potentials. This is the key result permitting one to study arrays with very large number of V_n 's.

The aforementioned solution method for G [49] readily gives the $R_{1,N}$ and $T_{1,N}$ coefficients of a collection of localized potentials by recursively regrouping the V_n 's ($n = 1, \dots, N$) into blocks. An example is given in Figs. 1(b) and 1(c), where $V_l, V_{l+1}, \dots, V_{n-1}$ are viewed as an unique localized potential $V_{n-1,l}$. So, for $R_{n-1,l}^{(\pm)}$, $T_{n-1,l}^{(\pm)}$ and $R_n^{(\pm)}$, $T_n^{(\pm)}$ the reflection and transmission coefficients, respectively, of $V_{n-1,l}$ and V_n [Figs. 1(b) and 1(c)], we have that

$$\begin{aligned} R_{n,l}^{(+)} &= R_{n-1,l}^{(+)} + \frac{R_{n-1,l}^{(+)} T_{n-1,l}^{(-)} T_{n-1,l}^{(+)} \exp[2ikd_n]}{1 - R_{n-1,l}^{(-)} R_n^{(+)} \exp[2ikd_n]}, \\ R_{n,l}^{(-)} &= R_n^{(-)} + \frac{R_{n-1,l}^{(-)} T_{n-1,l}^{(-)} T_n^{(+)} \exp[2ikd_n]}{1 - R_{n-1,l}^{(-)} R_n^{(+)} \exp[2ikd_n]}, \\ T_{n,l}^{(+)} &= \frac{T_{n-1,l}^{(+)} T_n^{(+)} \exp[ikd_n]}{1 - R_{n-1,l}^{(-)} R_n^{(+)} \exp[2ikd_n]}, \\ T_{n,l}^{(-)} &= \frac{T_{n-1,l}^{(-)} T_n^{(-)} \exp[ikd_n]}{1 - R_{n-1,l}^{(-)} R_n^{(+)} \exp[2ikd_n]}. \end{aligned} \quad (2)$$

For derivations refer to Refs. [51,53]. Here $d_n = a_n - b_{n-1}$.

The above relations will be fundamental for the developments next.

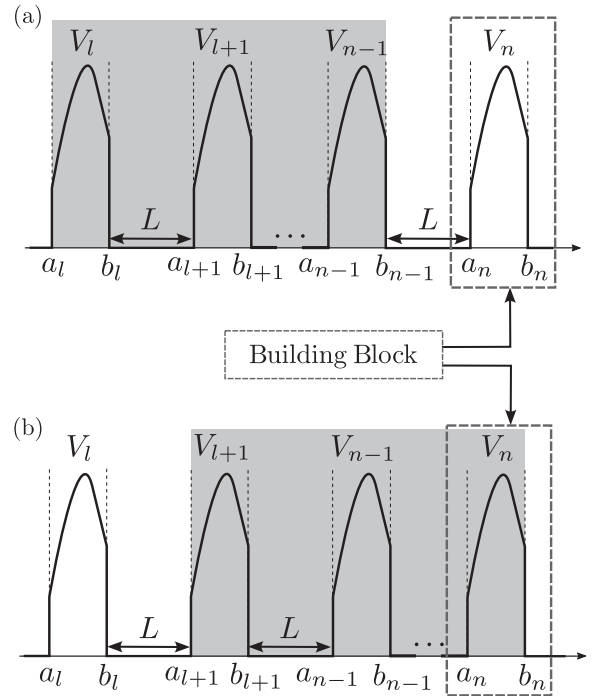


FIG. 2. A (finite) periodic structure compound of $N = n - l + 1$ localized potentials. (a) Block-barrier case. (b) Barrier-block case.

III. SCATTERING COEFFICIENTS AND CONTINUED FRACTIONS FOR PERIODIC STRUCTURES

We shall address long periodic lattices, so all the R_n 's and T_n 's are the same, whereas the r_n 's and t_n 's differ only by phases.

To establish a proper notation for our systems, let us recall basic facts about the scattering amplitudes r and t of an arbitrary single potential. We have that generally $t^{(+)} = t^{(-)} = t$ and $|r^{(\pm)}|^2 + |t|^2 = 1$ hence $|r^{(+)}|^2 = |r^{(-)}|^2$, moreover $r^{(\pm)*} t + r^{(\mp)} t^* = 0$. So, in terms of our previous R and T , $T^{(\pm)} = T$, $R^{(+)} = R$ and $R^{(-)} = R \exp[i\phi]$, with $\phi = 0$ for spatially symmetric compact support potentials (like a rectangular barrier, in opposition to a trapezoidal one, see later).

A. The recurrence relations for the reflection and transmission coefficients

Suppose a periodic finite array as depicted in Fig. 2, for which $N = n - l + 1$. By periodic we mean that the compound structure is formed by equally spaced $V_n = V$ ($n = 1, \dots, N$), with arbitrarily large, but finite, N . The compact support potential V is called the *building block* BB (or cell) of the this long finite lattice. The free regions (no potential) between the BBs correspond to $b_j < x < a_{j+1}$, with $l \leq j \leq n - 1$.

To derive recurrence relations for the reflection and transmission amplitudes of our full system, we particularize Eq. (2) to the situation where all the V_n 's are equal to V with $R^{(+)} = R$, $R^{(-)} = R \exp[i\phi]$ and T . Also, for simplicity hereafter R_M and T_M will refer to the scattering coefficients of a collection of M potentials V . Supposing the block-barrier configuration in Fig. 2(a), for the whole block of $N - 1$ potentials

we write $R_{N-1}^{(+)} = R_{N-1}$, $R_{N-1}^{(-)} = R_{N-1} \exp[i \Phi_{N-1}]$ and T_{N-1} . Thus, defining

$$g_M(\varphi) = 1 - R R_M \exp[i(2kL + \varphi)], \quad (3)$$

we find for $R_N^{(+)}$, $R_N^{(-)}$ and T_N

$$\begin{aligned} R_N &= R_{N-1} + \frac{R T_{N-1}^2 \exp[2ikL]}{g_{N-1}(\Phi_{N-1})}, \\ R_N \exp[i \Phi_N] &= R \exp[i \phi] \\ &\quad + \frac{T^2 R_{N-1} \exp[i(2kL + \Phi_{N-1})]}{g_{N-1}(\Phi_{N-1})}, \quad (4) \\ T_N &= \frac{T T_{N-1} \exp[ikL]}{g_{N-1}(\Phi_{N-1})}. \end{aligned}$$

Similarly, performing the computations for the barrier-block configuration in Fig. 2(b), we get

$$\begin{aligned} R_N &= R + \frac{T^2 R_{N-1} \exp[2ikL]}{g_{N-1}(\phi)}, \\ R_N \exp[i \Phi_N] &= R_{N-1} \exp[i \Phi_{N-1}] \\ &\quad + \frac{R T_{N-1}^2 \exp[i(2kL + \phi)]}{g_{N-1}(\phi)}, \quad (5) \\ T_N &= \frac{T T_{N-1} \exp[ikL]}{g_{N-1}(\phi)}. \end{aligned}$$

Above, $R_0 = 0$ and $T_0 = 1$ since one can regard $N = 0$ as the absence of V . For $N = 1$ we also should let $L \rightarrow 0$.

Once the structures in Figs. 2(a) and 2(b) are exactly the same, Eqs. (4) and (5) should agree pairwise. Therefore, for any N one finds by, respectively, comparing the last relations in Eqs. (4) and (5) and substituting the last in the first relation in Eq. (4), that

$$\begin{aligned} \Phi_{N-1} &= \phi, \\ T_N^2 &= \frac{(R_N - R_{N-1}) T^2}{R g_{N-1}(\phi)}. \quad (6) \end{aligned}$$

So, from a general formula for R_N and g_N we easily obtain T_N . By the same token, considering the definition of g_N and the second relation in Eq. (4), we get

$$\begin{aligned} g_N(\phi) &= 1 - R^2 \exp[i(2kL + \phi)] \\ &\quad - \frac{(1 - g_{N-1}(\phi)) T^2 \exp[2ikL]}{g_{N-1}(\phi)}, \quad (7) \end{aligned}$$

leading to R_N from Eq. (3).

B. The exact continued fraction solution

We shall solve Eq. (7). Thus, setting

$$\begin{aligned} \gamma &= \frac{1 + (T^2 - R^2 \exp[i \phi]) \exp[2ikL]}{iT \exp[ikL]}, \\ C_M &= \frac{g_M(\phi)}{iT \exp[ikL]}, \quad (8) \end{aligned}$$

we obtain for Eq. (7)

$$C_N = \gamma + \frac{1}{C_{N-1}}. \quad (9)$$

Hence C_N is the N -th term of a CF [54,55], or

$$C_N = \gamma + \frac{1}{\gamma + \frac{1}{\gamma + \frac{1}{\ddots \gamma + \frac{1}{C_0}}}}. \quad (10)$$

Note that $C_0 = 1/(iT \exp[ikL])$. Now, based on certain general properties of CF, as demonstrated in the Appendix A we can cast C_N as

$$C_N = \frac{(1 + C_0 \Gamma_-) \Delta^N - (1 + C_0 \Gamma_+)}{(C_0 - \Gamma_+) \Delta^N - (C_0 - \Gamma_-)}, \quad (11)$$

with

$$\Gamma_{\pm} = (\gamma \pm \sqrt{\gamma^2 + 4})/2, \quad \Delta = \Gamma_-/\Gamma_+. \quad (12)$$

Importantly, Eq. (11) has no limitations regarding N .

Finally, as a function of the auxiliary quantity C_N

$$\begin{aligned} R_N &= \frac{1 - C_N/C_0}{R \exp[i(2kL + \phi)]}, \\ T_N &= \sqrt{1 - C_N/C_{N-1}} \frac{T}{R} \exp[-i(kL + \phi/2)]. \quad (13) \end{aligned}$$

We directly have R_N and T_N by inserting Eq. (11) into Eq. (13). This allows to calculate the scattering by arrays of very large N 's through an easy to handle formula.

Interestingly, resonance k_{res} 's follow directly from the above expressions, with k_{res} meaning $|T_N(k_{\text{res}})|^2 = 1$ or $|T_N(k_{\text{res}})|^2 = 0$. They are akin to $R_N(k_{\text{res}}) = 0$ or $|R_N(k_{\text{res}})|^2 = 1$, which from Eq. (13) yield $C_N(k_{\text{res}}) = C_0(k_{\text{res}})$ or $|1 - C_N(k_{\text{res}})/C_0(k_{\text{res}})|^2 = |R(k_{\text{res}})|^2$. These global resonances can emerge either trivially, for the BB coefficients $|T(k_{\text{res}})|^2 = 1$ or $T(k_{\text{res}}) = 0$, or from proper perfect constructive or destructive interference due to multiple scattering along the N potentials V .

We end this section mentioning other CF approaches in the literature, however aimed to obtain R and T of a single localized potential. So, in a sense they are complementary to our present results. Very popular is the one originally developed in Refs. [36–38], where the scattering amplitudes can be written as CF. The calculations are performed interactively, stopping after the scattering amplitudes reach, in practice, a stationary condition. Another important procedure is that in Refs. [42,43], based on numerical implementations for a discretized Schrödinger equation, using CF for its solution. As far as we know such schemes have not being applied to lattice structures. Thence, in case one does not know the amplitudes R and T for the BBs of interest, one could employ these CF (or yet others, as TM) methods allied to the main expressions above to study long periodic structures.

C. Energy bands for 1D crystals: the $N = \infty$ limit

In terms of the auxiliary function C_N and the scattering coefficients of the BBs— R , $R \exp[i \phi]$ and T —the transmission and reflection probabilities for a lattice with N cells can be written as [see Eq. (13)]

$$|T_N|^2 = \left| 1 - \frac{C_N}{C_{N-1}} \right| \frac{|T|^2}{|R|^2}, \quad |R_N|^2 = \left| 1 - \frac{C_N}{C_0} \right| \frac{1}{|R|^2}. \quad (14)$$

Setting $F = (C_0 - \Gamma_-)/(C_0 - \Gamma_+)$, we have from Eq. (11)

$$\left| 1 - \frac{C_N}{C_{N-1}} \right| = \left| \frac{F(\Delta - 1)^2}{(1 - F/\Delta^N)^2 \Delta} \right| \frac{1}{|\Delta|^N}. \quad (15)$$

For $|\Delta| \geq 1$, the r.h.s of Eq. (15) goes to zero when $N \rightarrow \infty$. In this way, there is no transport along the lattice once then $T_{N=\infty} = 0$. So, in the infinite case, i.e., a 1D crystal, the allowed energy bands should follow from the complementary condition, or $|\Delta| < 1$.

From Eqs. (8) and (12), we get

$$\Delta = \frac{f(k) - i\sqrt{1 - f(k)^2}}{f(k) + i\sqrt{1 - f(k)^2}},$$

$$f(k) = \frac{\exp[-ikL]}{2T} + \frac{(T^2 - R^2 \exp[i\phi]) \exp[ikL]}{2T}. \quad (16)$$

Thus $|\Delta| < 1$ yields $f(k) < 1$, where $k^2 = 2mE/\hbar^2$. We now set the parametrization $\cos[q(L + d)]$, with q the crystal momentum and $d = b_n - a_n$ the width of the BBs. Thence, the energy bands read

$$\cos[q(L + d)] = \frac{\exp[-ikL]}{2T} + \frac{(T^2 - R^2 \exp[i\phi]) \exp[ikL]}{2T}. \quad (17)$$

The choice $\cos[q(L + d)]$ (instead, e.g., of $\sin[q(L + d)]$) justifies from the special case $R \rightarrow 0$ and $|T| \rightarrow 1$, for which we must have q equivalent to k . The exact Eq. (17) applies to arbitrarily shaped localized BBs or cells, thus expanding the standard expression for spatially symmetric BBs, for instance, as given in Ref. [56].

We should remark that for mathematical simplicity, so far in this contribution we have considered the one particle (energy domain) propagator in the free space of the BB potential array rather than a single particle propagator in the many-body medium. A traditional way to incorporate the latter situation in the band theory of solids is to assume the effective mass approximation [56]. In our construction, this can be directly implemented by supposing a distinct constant $m_{eff} = m_n$ within each localized V_n . This causes changes in the individual potentials coefficients T and R and thus in T_N and R_N of the whole structure. In the applications in Sec. IV below, the goal is to further develop the framework. Hence, to keep the analysis as straightforward as possible we maintain the free space assumption. Nonetheless, to make concrete comparisons with experimental results, we discuss how to introduce effective masses in our formulas in Sec. V.

Lastly, for particular heterostructures setups and materials, specially in low dimensions (for an overview and examples see, e.g., Refs. [57–59]), a high carriers density in the system may demand the Coulomb and other interactions to be taken into account. These contexts are of course outside the scope of the current approach.

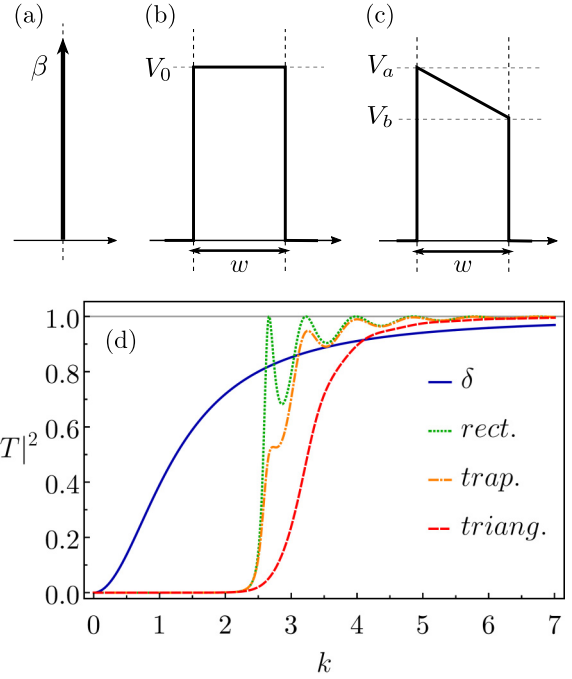


FIG. 3. Some single BBs: (a) Dirac delta, (b) rectangular, and (c) trapezoidal, potentials. For their strengths, here β , V_0 and V_a , V_b , positive (negative) values correspond to barriers (wells). The method properly works in both cases—Appendix C. (d) The transmission probability as a function of the incident (dimensionless) wavenumber k for four potentials. The (dimensionless) parameters for, respectively, δ , rectangular, trapezoidal and triangular barriers, are $\beta = 2.5$, $w = 3$ and $V_0 = 12$, $w = 3$ and $V_a = 8$, $V_b = 16$, and $V_a = 0$, $V_b = 24$. With the obvious exception of the delta, the parameters have been chosen so to lead to equal areas for all the other three barriers, thus yielding akin k ranges of variation for $|T|^2$. The β for the delta has also being set with such purpose.

IV. DISTINCT LATTICE STRUCTURE FEATURES AND THEIR SCATTERING PROPERTIES

In this section, we shall discuss very general scattering properties arising from different configurations for the BBs of a lattice. With such aim, specific values of parameters are not important, so here we consider dimensionless quantities, more convenient to make comparisons.

Thence, suppose \tilde{E} the energy, \tilde{m} the mass and $\tilde{\ell}$ a proper characteristic size of the system. For \tilde{q} (q) generally denoting a dimensional (dimensionless) physical variable, in our analyses we will consider: the wave number $\tilde{k} = \sqrt{2\tilde{m}\tilde{E}}/\hbar = k/\tilde{\ell}$, the potentials strengths $\tilde{V}_s = (\hbar^2/(2\tilde{m}\tilde{\ell}^2))V_s$ and the BB and lattice relevant lengths $\tilde{L} = \tilde{\ell}L$, $\tilde{w} = \tilde{\ell}w$, $\tilde{d} = \tilde{\ell}d$ (so that generally $\tilde{x} = \tilde{\ell}x$). In this way, for most of the plots we assume k , V_s , L , w , d and x .

A. Single building blocks (BBs)

To illustrate the method, we start considering the following single (in opposition to composed, see below) BBs: the Dirac delta, rectangular and trapezoidal potentials, Figs. 3(a)–3(c). The first two are symmetric, thus with $\phi = 0$, whereas the last is asymmetric if $V_a \neq V_b$. The scattering coefficients for

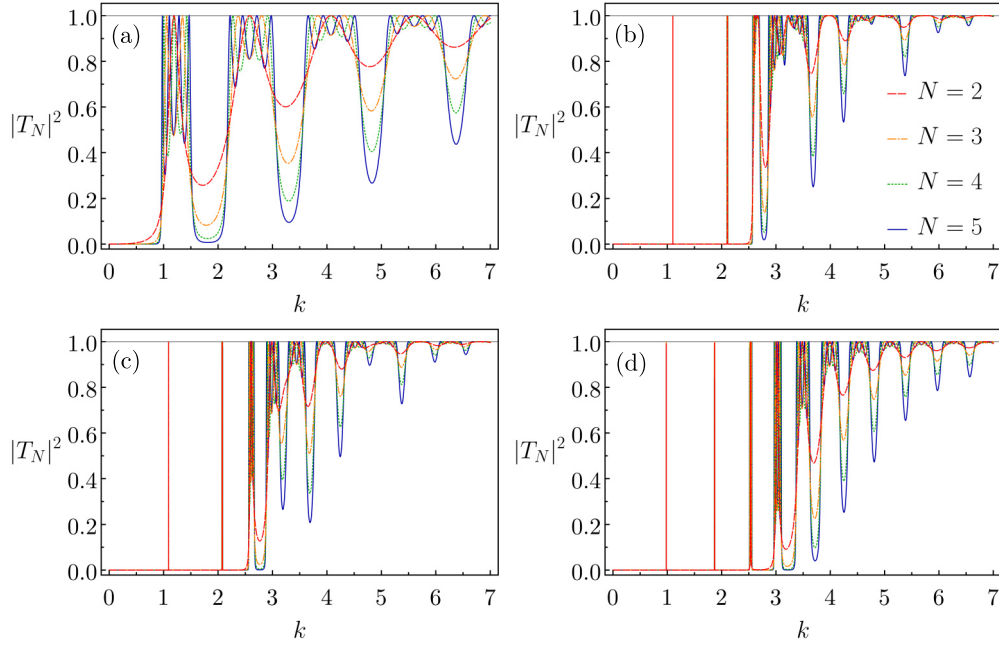


FIG. 4. Transmission probability as a function of k for finite structures formed by $N = 2, 3, 4, 5$ BBs, whose separation is always $L = 2$. The (a) Dirac delta, (b) rectangular, (c) trapezoidal, and (d) triangular barriers, with the same parameters of Fig. 3.

the delta and rectangular cases are readily found in textbooks. For arbitrary (dimensionless) wave number k , they read (with $\kappa = \sqrt{V_0 - k^2}$)

$$R_\delta = \frac{\beta}{2ik - \beta}, \quad T_\delta = \frac{2ik}{2ik - \beta},$$

$$R_{rect} = -\frac{i(\kappa^2 + k^2) \sinh[\kappa w]}{2\kappa k \cosh[\kappa w] + i(\kappa^2 - k^2) \sinh[\kappa w]},$$

$$T_{rect} = \frac{2\kappa k}{2\kappa k \cosh[\kappa w] + i(\kappa^2 - k^2) \sinh[\kappa w]}. \quad (18)$$

For the trapezoidal potential, Fig. 3(c), the exact coefficients are derived in Appendix B (refer also to Refs. [60,61]), so that

$$R_{trap}^{(\pm)}(k) = \frac{\mathcal{D}^{(\pm)}(k)}{\mathcal{C}(k)}, \quad T_{trap}(k) = -\frac{2\eta(k)}{\pi \mathcal{C}(k)}. \quad (19)$$

The functions $\mathcal{D}^{(\pm)}(k)$, $\mathcal{C}(k)$ and $\eta(k)$ are given in Appendix B, involving Airy functions and their derivatives. Note that the rectangular (right triangular) potential corresponds to $V_a = V_b$ (either $V_a = 0$ or $V_b = 0$).

Profiles of the transmission probabilities $|T|^2$ as a function of k (of course $|R|^2 = 1 - |T|^2$) for the four BBs are depicted in Fig. 3(d). The parameters have been chosen so to facilitate qualitative comparisons between the potentials (with all the $|T|^2$, including the delta, being close to 1 around the same k intervals). First, the delta with the triangular and the rectangular with the trapezoidal tend to be more similar. Second, the delta presents the fastest raising (from $k = 0$) for the transmission probability, a consequence of its null width. Lastly, the trapezoidal mismatch of V_a and V_b can generate “local motifs,” as the shoulder seen for $k \sim 2.5$ in Fig. 3.

Although idealized potentials, we should recall the usefulness of such single BBs, justifying their choice here. For instance, Dirac delta barriers have long being employed to

model diverse quantum phenomena [62,63]. More recently, delta interactions have even found novel applications, like in the study of topological effects in 1D lattices [64] and the production of entanglement by the scattering of distinguishable [65] and free fermions [66] particles in 1D structures. The same is obviously true for rectangular barriers, specially in the effective description of materials [67]. As illustrations, rectangular barrier networks have been used to simulate gallium arsenide semiconductor superlattices [68], as well as to investigate conductance in multi-junction solar cells and in layered graphene [10,13]. Trapezoidal and triangular barriers have also been considered to analyze charge transport in oxides [69–71], as in the case of thin aluminum oxides films and ultra-thin gate dielectrics [69,70]. Also, these potentials have been employed to explain scanning tunneling microscope (STM) data related to materials surface properties [72]. Furthermore, a good agreement between experiments and simulations of perovskite ferroelectric tunnel junctions (based on trapezoidal potentials) have been reported [73].

Supposing the above four BB potentials—delta, rectangle, trapezoid and right triangle—we discuss some finite lattices. As a first illustration, we present examples with $N = 2, 3, 4, 5$ cells assuming the same parameters values of Fig. 3. The resulting $|T_N|^2$ as a function of k are shown in Fig. 4. Few general trends can be identified. For instance, consider $k > 1$, $k > 2.5$, $k > 2.5$ and $k > 3$, respectively, in Figs. 4(a)–4(d). Then in these k intervals, qualitatively the triangular, Fig. 4(d), is closer to the delta, Fig. 4(a), than to the trapezoidal, Fig. 4(c), case. Intuitively, we can understand this by observing that the delta and triangular barriers have both “pointed” shapes and consequently—as previously mentioned—fairly overall similar behavior (although not for the transmission initial increasing onset) for the individual R ’s and T ’s, see the corresponding plots in Fig. 3. Also, a certain resemblance exists between the rectangular, Fig. 4(b), and trapezoidal, Fig. 4(c),

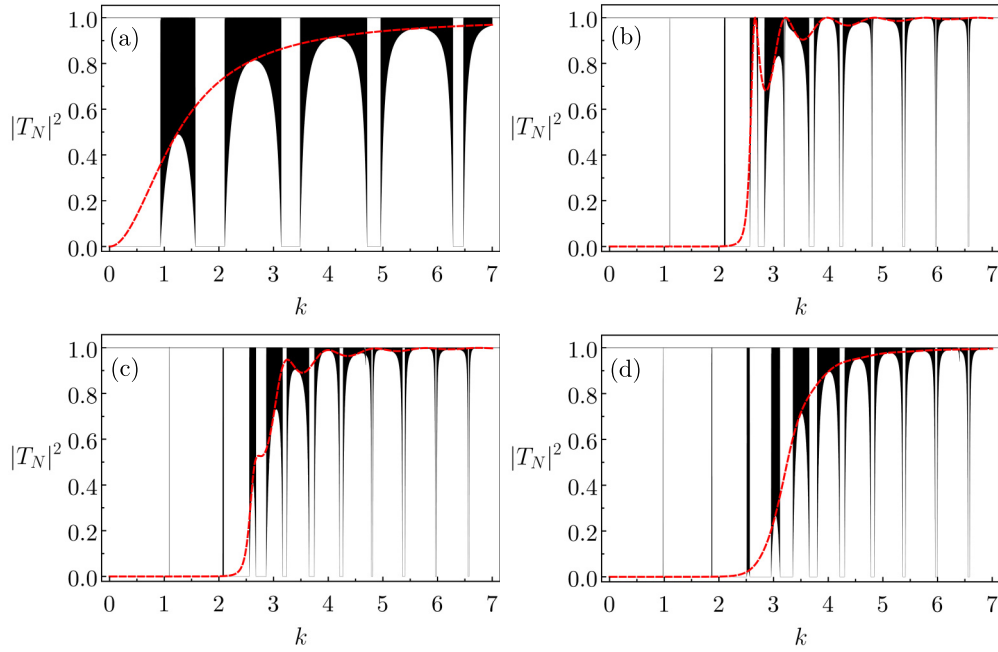


FIG. 5. The same than in Fig. 4, but with $N = 10^{10}$ for the (a) delta and $N = 10^6$ for the (b) rectangular, (c) trapezoidal, and (d) triangular barriers. The dashed curves refer to the case of $N = 1$ ($|T|^2$ for just a single potential).

cases, specially for greater k 's, when the height difference between V_b and V_a for the latter becomes less relevant.

We remember our method is exact. Hence, in principle there is no need to discuss numerical accuracy issues. Nonetheless, few comparisons with the literature would be instructive. They are presented in Appendix C, where we consider some previous works addressing up to $N = 100$ BBs. However, with our framework we can calculate lattices with orders of magnitude greater N 's. This is exemplified in Fig. 5, where $N = 10^{10}$ for the delta and $N = 10^6$ for the other three types of BBs. Again, the parameters are the same than in Fig. 3. We remark the computations for each case took less than 5 minutes in a very simple personal computer—with a i5 processor—by implementing an extremely fine (not really necessary and done just for benchmark purposes) variation of k , roughly 700 000 (delta) and 493 000 (other potentials) values in the numerical interval $0 \leq k \leq 7$. As expected, for so large N 's we already identify band structures, which for many practical purpose are those of the actual infinite lattices. For instance, as we have checked the allowed band widths and edges agree with Eq. (17), results not shown. Also, contrasting Figs. 4 and 5, we see that the forbidden bands (the k ranges in which $T_N = 0$) become very well defined. Moreover, general trends discussed in the literature (e.g., refer to Ref. [19]) are likewise observed here. Indeed, the corresponding single BB $|T(k)|^2$ curve tends to touch the center points of all the allowed bands [19], Figs. 5(a)–5(d). On the other hand, the BB transmission probability $|T(k)|^2$ clearly plays the role of an envelope for the mentioned points only for the sharpening delta, Fig. 5(a), and triangular, Fig. 5(d), barriers. Lastly, using as a guide the allowed bands seen in Fig. 5, Fig. 4 illustrates that within any of these band regions we have $N - 1$ k 's for which $|T_N|^2 = 1$. Although this can be understood from the formal derivations in [19], a

more intuitive explanation relates to the system quasibound states (characterized by $|T_N|^2 = 1$). Given that for N BBs the resulting large but finite array can be thought of as formed by $N - 1$ no confining wells, we get groups of $N - 1$ quasibound states in certain ranges of k , exactly those corresponding to the allowed bands. As we have checked numerically, this is also the case for the very narrow peaks in the region $k < 2.5$ in Figs. 4(b)–4(d). As an example, for $N = 5$ trapezoidal barriers, we have $|T_5(k)|^2 = 1$ for k equals to 1.09255, 1.09295, 1.09344, 1.09383, and 2.07026, 2.07524, 2.08166, 2.08710, associated, respectively, to the first and second sets of extremely closed together peaks in Fig. 4(c).

A more complete analysis of the bands formation as N increases in the particular case of delta barriers [for the same parameters values of Fig. 4(a)] is presented in Fig. 6. First, we remark that for an actual crystal, in the k forbidden regions the transmission probability would be zero, abruptly changing to one at the allowed bands onsets. For N finite but large enough, we would have $|T_N|^2 \approx 0$ in certain k ranges and then $|T_N|^2$ sharply raising in the mentioned bands edges (for a nice discussion about the involved $|T_N|^2$ behavior as one go further into the k allowed regions when $1 \ll N < \infty$, see [19]). Thus the variation of $|T_N|^2$ from 0 to 1 should become sharper and sharper as N grows. This is indeed observed in Fig. 6(a), where we show how the bands emerge as N gets larger. Also as expected, a rapid transition from 0 to 1 of $|T_N|^2$ tends to demand greater N 's for higher k 's. For instance, for $N = 10$ in Fig. 6(a), we observe a very steep slope for $|T_{10}|^2$ about $k = 1$, nonetheless a relatively smoother slope about $k = 5$. Extra details are given in Figs. 6(b)–6(e), which magnify the ending or beginning of a forbidden band, taking place for k around, respectively, 0.93075 (ending), 2.10638 (ending), 3.14159 (beginning), 6.28318 (beginning). Notice that Fig. 6(b) displays the ending of the first forbidden band

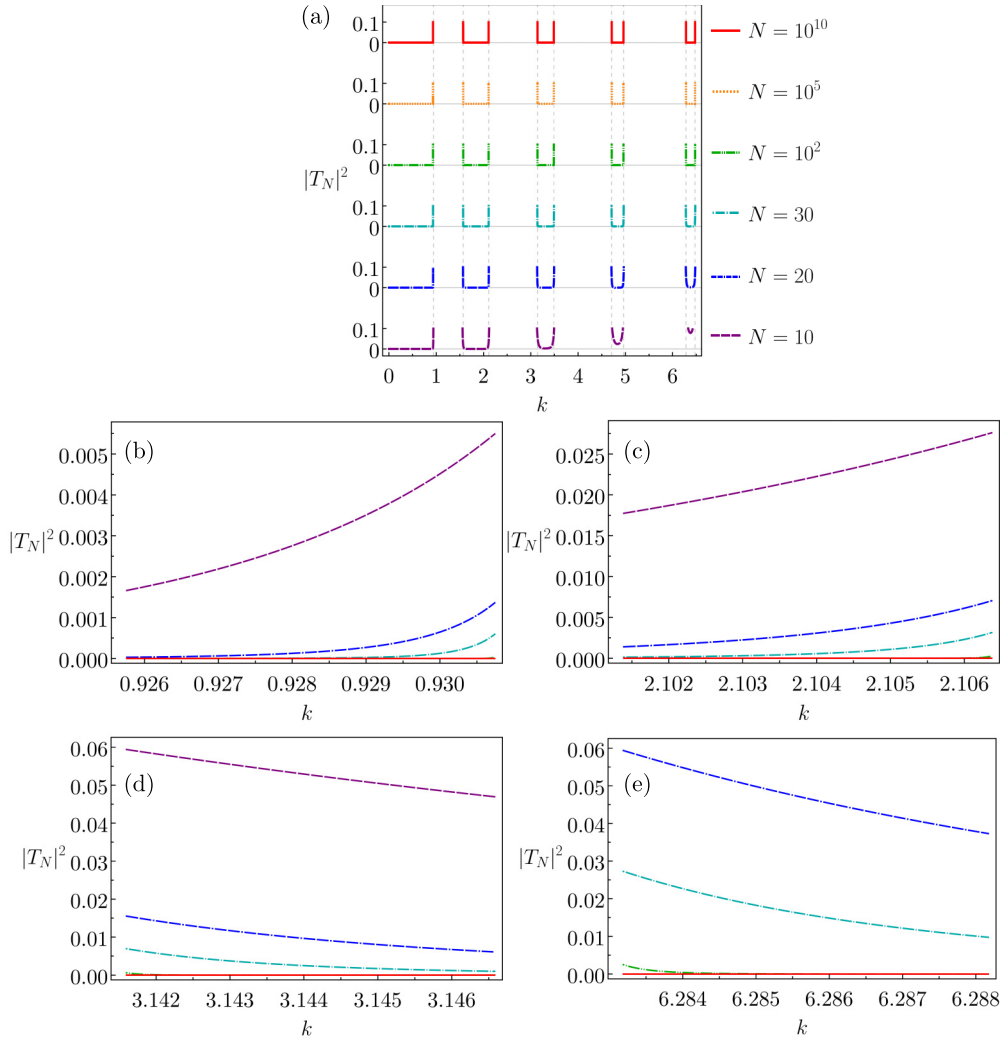


FIG. 6. The transmission probability as a function of k for arrays of N equally spaced delta barriers of parameters as in Fig. 4(a). For distinct N 's, in (a) plots highlighting only the k ranges where $|T_N|^2$ is rather small, so in the limit of N large comprising the system forbidden bands. For different N 's, graphs of $|T_N(k)|^2$ in short k intervals corresponding to the ending or beginning of a forbidden band at (b) $k \approx 0.93075$ (ending), (c) $k \approx 2.10638$ (ending), (d) $k \approx 3.14159$ (beginning), and (e) $k \approx 6.28318$ (beginning).

at around $k = 0.93075$, so a low k value. In this case, the transmission probabilities curves for $N = 10$ and 10^{10} differ by a factor of only 10^{-3} . On the other hand, in Figs. 6(c) and 6(d), for the ending and starting of the second and third forbidden bands, such difference is of $\sim 3 \times 10^{-2}$ and $\sim 6 \times 10^{-2}$. Moreover, in Fig. 6(e), the curve for $N = 10$ is not even present, since for such N the fifth forbidden band has not been properly formed yet.

As a last comment, we notice that the starting of the forbidden bands are always at $k_* = l\pi/L$, with $l = 1, 2, \dots$. This agrees with exact results obtained from the dispersion relation formula for the Dirac comb model (see, e.g., Refs. [19,21]). As demonstrated in the Appendix D, from the present method one likewise can obtain analytically such onsets for the zero transmission regions.

B. Composed building blocks (CBBs)

Next we consider lattices whose BBs are compositions of more than one localized potential, from now on referred

as CBBs. As workable examples we suppose CBBs formed by our previous four basic barriers, organized in a specified order (from left to right) V_1, V_2, \dots, V_p . We furthermore set the separation between V_1 and V_2 as $d_{12} = a_2 - b_1$, between V_3 and V_2 as $d_{23} = a_3 - b_2$ and so on. The exact reflection $R_{\text{CBB}}^{(\pm)}$ and transmission T_{CBB} coefficients for a given CBB are derived directly from the general Eqs. (2). Once we determine the actual expressions for $R_{\text{CBB}}^{(\pm)}$ and T_{CBB} , we just follow the protocol in Sec. III to solve the lattices formed by such CBBs.

We start addressing few aspects concerning nonsymmetric CBBs, arising when they are constructed from the same group of V 's, but in different dispositions. For so, we assume just two, rectangular and trapezoidal, potentials arranged in the two distinct ways depicted in the inset of Fig. 7(a). The nomenclature CBB-rt (CBB-tr) refers to the case where the rectangular (trapezoidal) potential comes first. Although we set an unique $d_{12} = d$ for both CBBs as well as the same parameter values for the individual rectangular and trapezoidal barriers, clearly CBB-rt and CBB-tr are not specular images of each other. The contrast between the two is easily

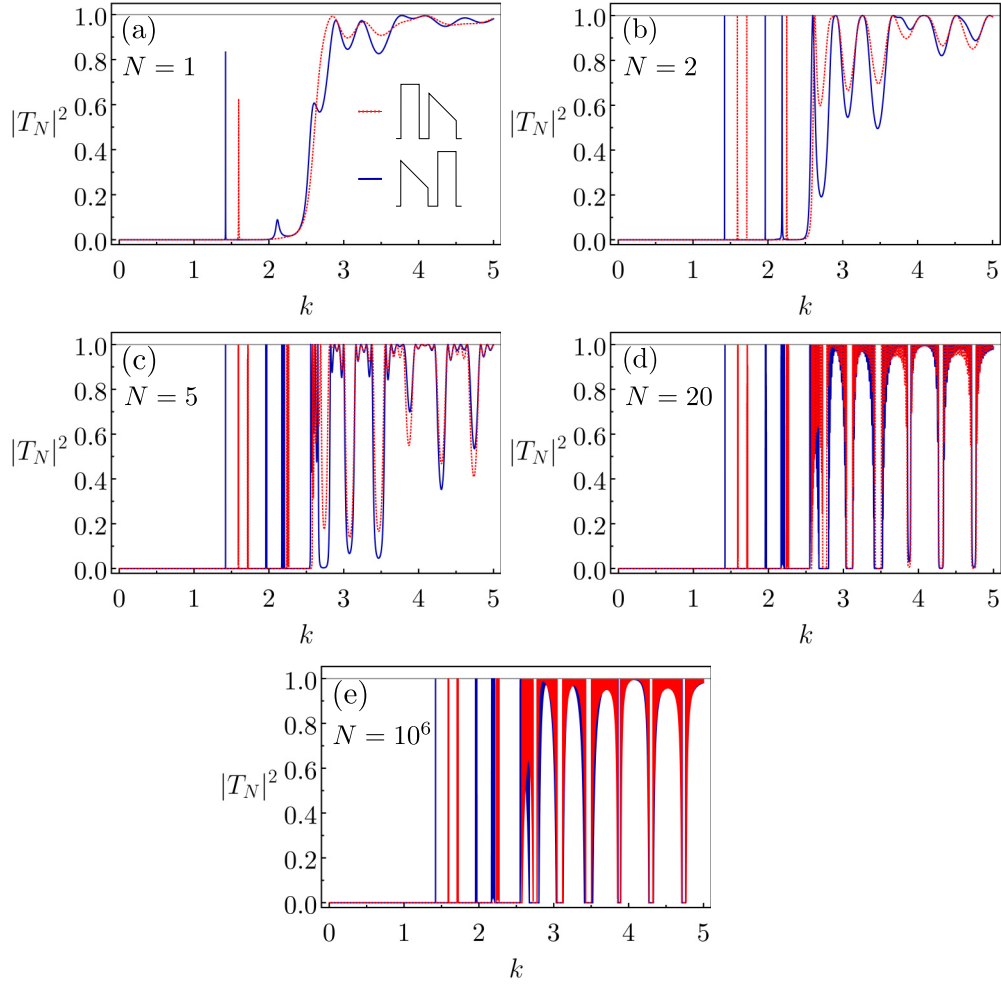


FIG. 7. Transmission probability for an unique (i.e., $N = 1$) CBB-rt and CBB-tr in (a) and for finite lattices formed by distinct number N of these CBBs in (b)–(e). In all cases, $d = 1$ and $L = 0.5$. For the rectangular and trapezoidal barriers the parameters are, respectively, $V_0 = 12$ and $w = 2$, and $V_a = 10$, $V_b = 4$, and $w = 3$.

observed from the plots of $|T_{\text{CBB}}|^2 = |T_{N=1}|^2$ for CBB-rt and CBB-tr shown in Fig. 7(a). Note, e.g., the distinct positions and heights of the first peak in their transmission probabilities. Phenomenologically, this relates to a dissimilar “internal” region, namely, that between the two barriers. Indeed, for the CBB-rt the higher side of the trapezoidal is spatially turned to the rectangular potential, whereas for the CBB-tr it is the lower side which faces the rectangular potential. Consequently, the interference patterns build up from the multiple scattering between the two localized V ’s — as calculated from the Green’s function method—result in distinct transmission and reflections profiles for CBB-rt and CBB-tr.

By considering an arrangement of N equally spaced (by L) CBB-rt and CBB-tr, we plot in Figs. 7(b)–7(e) the corresponding $|T_N|^2$ as function of k in the cases of $N = 2$, $N = 5$, $N = 20$ and $N = 10^6$. In such plots $L = d/2$. As in Sec. IV A, for the very large $N = 10^6$, we observe band-like structures. Furthermore, regardless the N ’s, overall the transmission profiles of CBB-rt and CBB-tr are not equal. But for $N = 10^6$ (and in a lesser extent, for $N = 20$), we see that in the present k interval, the difference between CBB-rt and CBB-tr tends to decrease as k increases. All these traits are not just artifacts

of special values of d and L . This is illustrated in Fig. 8, considering $|T_{N=10^6}|^2$ for $L = 10d$ with $d = 1$ and for $d = 10L$ with $L = 1$. Again, the transmission patterns are distinct for CBB-rt and CBB-tr.

It is worth remarking that modifications in band structures due to distinct arrangements of spatially asymmetric barriers, as above, have long ago been observed in processes like electronic scattering from ions with localized magnetic moments under an applied magnetic field [74]. More recently, it has been pointed out that technologically significant (for the development of various devices) physical effects such as, filters, diodes, one-way mirrors, and even more exotic Maxwell demons and invisibility cloaks, can be achieved from scattering asymmetries [75].

Another possible usage for CBBs is to build “compact” localized symmetric potentials, whose particular shapes may be of potential interest in different contexts (see below). For instance, two equal right-triangular barriers when specularly juxtaposed (i.e., the right angle sides facing each other without any spacing between them) creates an isosceles-triangular barrier, as depicted in the inset of Fig. 9(a). Likewise, the juxtaposition of a right-triangular barrier, a rectangular barrier and

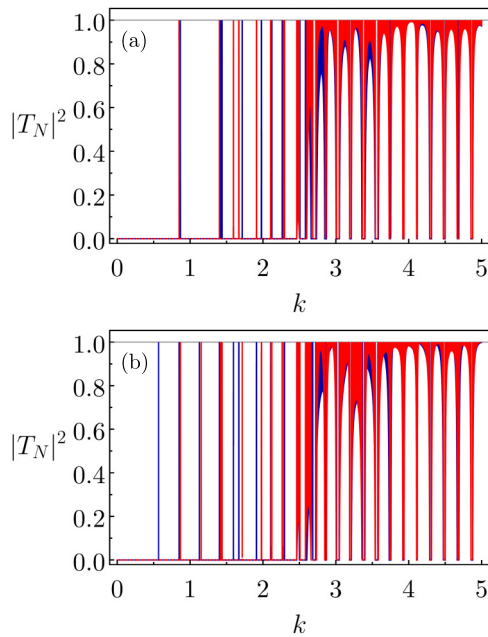


FIG. 8. The same than in Fig. 7, but only for $N = 10^6$ and (a) $L = 10d$ with $d = 1$ and (b) $d = 10L$ with $L = 1$.

then an akin (but flipped) right-triangular barrier—all having the correct proportions—produces an isosceles-trapezoidal barrier, represented in the inset of Fig. 9(b). In all these cases the exact T_{CBB} and R_{CBB} are derived from our previous Eq. (2),

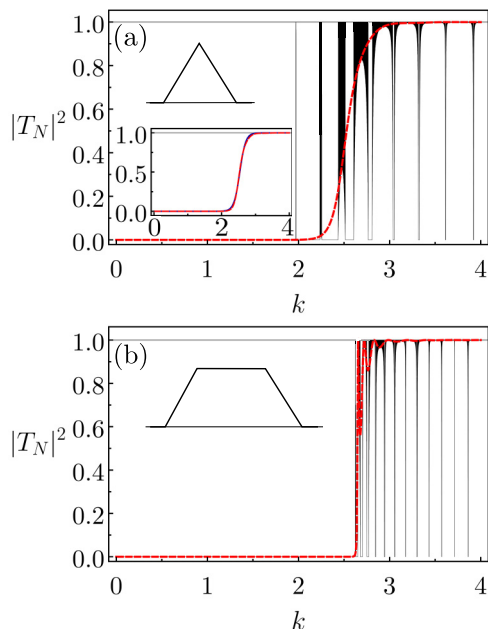


FIG. 9. Transmission probabilities for an unique (dashed curves) and arrays with $N = 10^6$ (continuous curves) CBBs shown in the insets. For the lattices, the spacing is $L = 1$. Also, in both cases the maximum height is $8\sqrt{3}$. (a) For the isosceles-triangular barrier, the base length is 4, whereas (b) for the isosceles-trapezoidal barrier, the bases lengths are 8, top, and 12, bottom. In detail in (a) the good fitting of a sigmoid function to $|T_{\text{CBB}}|^2$ (see main text).

setting the d_{nn+1} 's to zero. The corresponding transmission probabilities are shown in Fig. 9. Similar to the delta and triangular barriers, $|T_{\text{CBB}}|^2$ for the isosceles-triangle increases monotonically with k , consequence of its edged format. In particular, it can be approximated by a sigmoid function $(1 + \exp[-\nu(k - \xi)])^{-1}$, which for the parameters values in Fig. 9(a) lead to $\nu \approx 11.56$ and $\xi \approx 2.54$ —the resulting good fit is shown in the inset of Fig. 9(a). In Fig. 9, we also show periodic arrays with $N = 10^6$ of these compact composite potentials, assuming a separation of $L = 1$ between the CBBs. The band structure of the isosceles-triangular barriers array resembles that of the right-triangular system in Fig. 5(d). For other works analyzing sharpened barriers in setups similar to ours, we mention [61,76] (the former considering the action of a constant electric field). By its turn, the band structure for the isosceles-trapezoid does not follow the exact same features of either the rectangular or the right-trapezoidal layouts, respectively, in Figs. 5(b) and 5(c).

The localized potentials in Fig. 9 have been considered in the investigation of heterostructures formed by GaAs quantum wells and $\text{Al}_x\text{Ga}_{1-x}\text{As}$ barriers [77], but in arrays with only $N = 10$ building blocks. Moreover, such work supposes BenDaniel-Duke boundary conditions and the effective mass approximation. The calculations were performed using the TM method. Despite these differences, the qualitative results are fairly similar to the ones here. We observe that presently we are working on extensions of our protocol to include arbitrary boundary conditions within the effective mass approximation. Hopefully, such generalizations will be reported in the near future. We also should mention that special profiles for the diffracting elements in optical gratings, as triangular-like shapes, can give rise to rich phenomena [78]. Conceivably, this also could be the case for electrons in lattices formed by isosceles-triangular barriers (see, e.g., Ref. [61]).

V. TWO CONCRETE APPLICATIONS

Typically, a certain number of semiconductors materials are used to build the successive layers in heterostructures. Thus, for an electron propagating in a given slab, one should consider the corresponding bulk properties, in special the constant effective mass and the conduction band edge, whose offsets between adjacent layers define the relative heights of the barriers interfaces. In this way, we can associate the material with the lowest conduction band edge in an actual heterostructure to the “background medium”—the one for which $V = 0$ —of our periodic structures in Sec. II (refer to Fig. 2). The remaining materials are therefore related to the localized potentials forming the BBs.

The above are simply introduced into our previous formulation through straightforward re-scaling of the individual localized potentials transmission and reflection amplitudes forming the BBs. All the other expressions remain the same. So, suppose R and T the scattering coefficients for an arbitrary potential $V(x)$, non-null only in the interval $I : a < x < b$ and for the mass, m , being the same everywhere. Now, if we have an energy profile such that the minimum onset is not 0 but V_0 and outside I the effective mass is m_0 , then we can use akin formulas for R and T , but instead

of E , $k(0)$ and $\kappa(x) = \sqrt{2mV(x)/\hbar^2 - k(0)^2}$, with $k(U) = \sqrt{2m(E - U)/\hbar^2}$, we take E' , k' , and κ' where $E' = E - V_0$, $k' = \sqrt{m/m_0}k(V_0)$ and $\kappa'(x) = \sqrt{2mV(x)/\hbar^2 - k(V_0)^2}$. As an example, useful in the applications below, for a rectangular barrier the particular expressions for R and T in Eq. (18) should be changed exactly in this way, setting $m = m_j$ and $V(x) = V_j$ for the layer j .

A. Optimizing transport in heterostructures for solar cells applications

The transport properties in multijunction semiconductor compounds—so displaying different band-gaps—is a key aspect in the functioning of distinct purpose devices. In the particular case of solar cells, this type of structure has been largely studied due to its low-cost of fabrication and the promising conversion efficiencies, expected to exceed 50% [79,80]. However, such a high performance depends, among other factors, on the semiconductors crystal quality and a proper combination of the employed materials parameter values.

For instance, in Ref. [13] it has been proposed that a strain-balanced GaAsSb/GaAsN superlattice is a suitable system for solar cell applications. The geometry is depicted in Fig. 10(a), where one has successive layers made of GaAsSb, the “barriers” and GaAsN, the “background medium” (or “wells”). For these materials, the effective masses [81] are $m_1^* = 0.067 m_e$ (for GaAsSb_{0.0325}) and $m_0^* = 0.098 m_e$ (for GaAsN_{0.012}), with m_e the electron rest mass (these are the actual concentrations used in Ref. [13]). Further, the barrier heights are around $V_1 \sim 1.41$ eV and $V_0 \sim 1.13$ eV [82,83]. The widths, d and L , are then the free parameters which could be optimized, seeking to enhance the transport properties. Indeed, the experimental results in [13] show that solar cells with smaller $d + L$ periods (tested for samples with $d = L$) tend to present higher efficiencies. Calculations using the TM technique for $N = 12$ cells in the case of $d = L$ corroborated these findings [13]. The analysis in Ref. [13] considered the approximation of a same effective mass in both materials (set to $0.146 m_e$) and a relative barrier height of 250 meV (so, a bit distinct from the value we employ here, of $\Delta V = V_1 - V_0 = 280$ meV, see Fig. 10).

Using our present method for the structure in Fig. 10(a), in Fig. 10(b) we display the computed transmission probability as function of d and L for a 200 nm thick heterostructure (the samples sizes in Ref. [13]), associated to a network with $N \approx 200 \text{ nm}/(d + L)$ BBs (for instance, for $d = 3$ nm and $L = 2$ nm, $N = 40$). As the incident energy we set $E = \Delta V/2$. Notice there is a considerable transmission for smaller d 's, but not necessarily for smaller L 's. From the plots one clearly sees that for greater transport one should have the GaAsSb layers with $d \lesssim 3$ nm, but the GaAsN slabs may be thicker, e.g., for the L 's multiples of 5 nm, Fig. 10(b). In addition, to set $d = L$ [the solid line in Fig. 10(b)] might constitute a restrictive condition in certain applications. However, Fig. 10(b) indicates that devices with $d < L$ can likewise display good efficiency, in agreement with [81].

These structures energy bandgaps as a function of the period $d + L$ are presented in Fig. 10(c), for $d = L$. The square

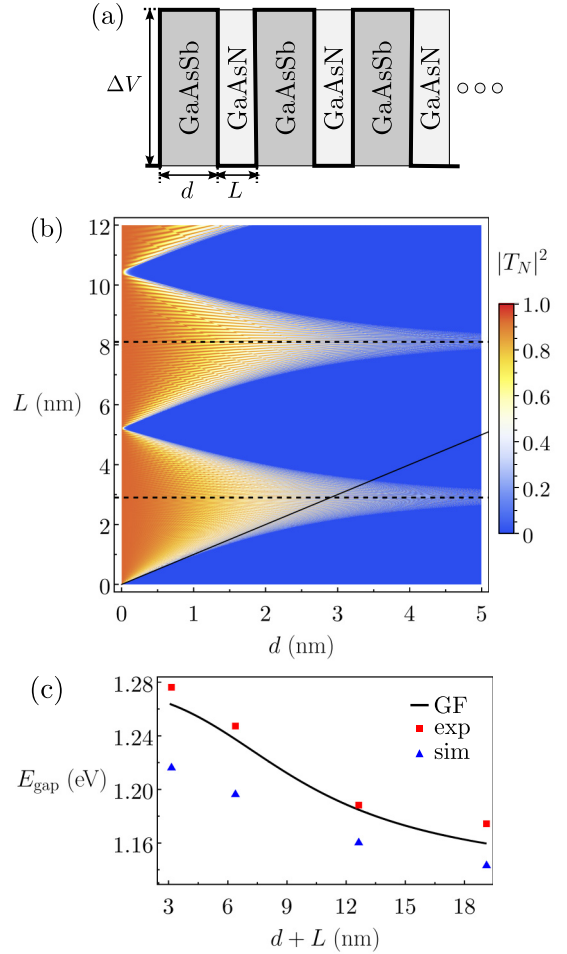


FIG. 10. (a) Schematics of the successive GaAsSb/GaAsN layers forming a rectangular superlattice (aimed for solar cell devices). (b) Transmission probability, calculated from the present approach, as a function of d and L for a 200 nm thick sample, so with a number N of BBs or cells given by $N \approx 200/(d + L)$. Here $E = (V_1 - V_0)/2 = \Delta V/2$, see main text. (c) The superlattice energy bandgap as a function of the period ($d + L$) obtained from the experiments (exp) and simulations (sim) in [13] and from the Green’s function procedure (GF).

(triangular) symbols correspond to the experimental data (simulations) in Ref. [13], obtained through photoreflectance measurements (finite difference method). As expected, as the period $d + L$ increases, the bandgap decreases. The continuous curve represents our Green’s function framework [whose computations are exactly as those described in Sec. IV, here for the structure in Fig. 10(a)], which closely reproduces the experiments. Comparing the GF results and the corresponding four data points, we obtain the following percentage errors: 1.01%, 0.80%, 0.29%, and 1.25%, listed from the lowest to the highest period considered in the experiments. By calculating the number of cells N as previously described, the actual structures yield approximately 63.57, 31.31, 15.83, and 10.46. When the noninteger part of these values is close to 0.5, it indicates that in the sample there is an additional barrier [GaAsSb layer, first half of the period $d + L$, see Fig. 10(a)] in the structure. Conversely, when the

noninteger part approaches 0 or 1, there is a more balanced distribution of “barriers” (GaAsSb) and “wells” (GaAsN). This observation partially explains the distinct percentage errors, which are higher in the extreme period values, reflecting a greater imbalance between the barriers and wells.

We end this section mentioning we have tested much longer structures, for N 's around thousands (graphs not shown). Qualitatively, all the results obtained are essentially the same than the ones in Fig. 10.

B. Band-pass transmission by mode coupling: The case of asymmetric barriers

A band-pass filter (BPF) is a long known effect in unidulatory processes. More than two decades ago pioneer works have studied such phenomenon for electrons in finite semiconductor heterostructures [84–86]. Recently, band-pass electronic transmission have been considered, e.g., to maximize the conversion efficiency in thermoelectric generators [87]. Certain realizations are based on nanowire quantum dots [88], theoretically modeled as rectangular superlattices [89,90]. General features of these BPFs are greatly determined by the networks unitary cells properties. For example, an interesting mechanism responsible for the creation of BPFs, unveiled in Ref. [29], relates to the coupling of resonant modes, with a good fraction of them being associated to the lattice BBs. Hence, to characterize these types of BPFs one needs to properly identify and classify the distinct resonances in heterostructure [29].

As mentioned in Sec. III B, our present method allows to analytically single out transmission resonances, even when the BBs are formed by various materials, something harder to achieve from other protocols. So, motivated by the above discussion, here we shall address a key resonant mode discussed in Ref. [29], that linked to the compound unitary cell in the Fabry-Pérot condition.

Thus let us assume a single semiconductor rectangular barrier of relative height $V_j - V_0$, effective mass m_j and width $d_j = w$ (outside the slab, we suppose the effective mass being m_0 everywhere). From Eq. (18), we can write

$$\begin{aligned} T_j &= 1/A_j, & R_j &= -B_j/A_j, \\ A_j &= \cosh[\kappa'_j w] + \frac{i}{2} \left(\frac{\kappa'_j}{k'} - \frac{k'}{\kappa'_j} \right) \sinh[\kappa'_j w], \\ B_j &= \frac{i}{2} \left(\frac{\kappa'_j}{k'} + \frac{k'}{\kappa'_j} \right) \sinh[\kappa'_j w]. \end{aligned} \quad (20)$$

The above expressions show that for specific energies, full transmission is achieved when ($n = 1, 2, \dots$)

$$\kappa'_{j,\text{res}} w = i n \pi. \quad (21)$$

Equation (21) represents the Fabry-Pérot (FP) resonance condition for an isolated barrier. One gets a 100% transmission along a whole heterostructure if its cells meet the FP condition at particular resonance energies.

Now, we examine a lattice whose CBB is formed by two rectangular semiconductor layers, labeled as 1 and 2, and spaced by a “background medium” (another semiconductor material) of width ℓ , see Fig. 11(a). From Eq. (2) their com-

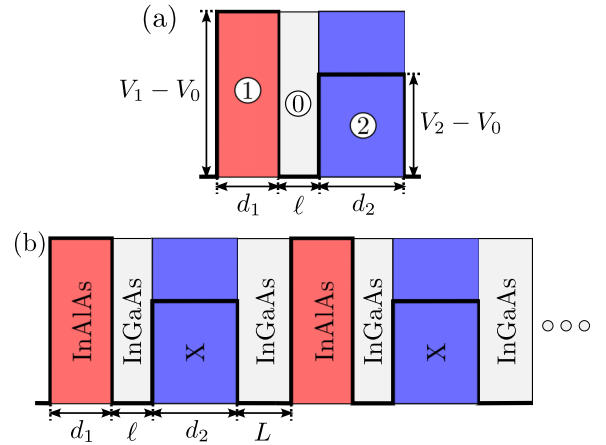


FIG. 11. (a) Schematics of a CBB formed by three semiconductor layers, the middle one representing the “background medium,” and their respective parameters. (b) A InAlAs/InGaAs/X superlattice, whose barriers composing the unitary cell (BB) have widths d_1 , ℓ , and d_2 . The BB spacing is L .

bined transmission \mathcal{T} and reflection \mathcal{R} coefficients read

$$\begin{aligned} \mathcal{T} &= 1/A, & \mathcal{R}^{(\pm)} &= -\mathcal{B}^{(\pm)}/A, \\ A &= A_1 A_2 \exp[-i k' \ell] + B_1 B_2 \exp[i k' \ell], \\ \mathcal{B}^{(+)} &= A_2 B_1 \exp[-i k' \ell] + \frac{B_2}{A_1} (1 - B_1^2) \exp[i k' \ell], \\ \mathcal{B}^{(-)} &= A_1 B_2 \exp[-i k' \ell] + \frac{B_1}{A_2} (1 - B_2^2) \exp[i k' \ell]. \end{aligned} \quad (22)$$

For this problem, we can have three different situations. The trivial one is that for which materials 1 and 2 are the same and the widths $d_1 = d_2 = w$. Then, in fact the lattice is formed by a simple BB, a rectangular barrier, and the FP resonance for the full structure is given directly by Eq. (21).

The second is when the materials are again the same (say, material 1), but $d_1 \neq d_2$. This is the case investigated in Ref. [29]. If we choose the barriers thicknesses such that $d_1 = n_1 w$ and $d_2 = n_2 w$, for n_1 and n_2 positive integers, we find that for energies satisfying Eq. (21) (with $j = 1$), it follows from Eq. (22) that

$$|\mathcal{T}(\kappa'_{1,\text{res}})|^2 = 1, \quad \mathcal{R}^{(\pm)}(\kappa'_{1,\text{res}}) = 0. \quad (23)$$

Thence, the CBB—consequently the entire heterostructure—obeys a FP transmission resonance condition akin to that of its isolated rectangular barriers, regardless the values of ℓ and L . This is one the results obtained in [29], but here derived in a rather straightforward way.

Finally, for materials 1 and 2 distinct—as far as we know a context for FP resonances not addressed before in the literature—the analysis is as the following. We must have $E(\kappa'_{1,\text{res}}) = E(\kappa'_{2,\text{res}})$ if ℓ must not have a role in the resonances—remember that quasi-states-like modes for the CBB will depend on the “well” size ℓ , Fig. 11(a). We can write $d_2 = \alpha d_1$ and for sake of definiteness to set $V_1 > V_2$. Then,

TABLE I. The bulk parameters of the materials forming the InAlAs/InGaAs/X heterostructure, with $X = \text{GaAsSb}$ or $X = \text{InP}$ [91]. The reference potential height V_0 refers to InGaAs.

Material	Index j	m_j/m_e	$V_j - V_0$ (meV)
InGaAs	0	0.041	0
InAlAs	1	0.078	520
InP	2	0.079	180
GaAsSb	2	0.040	360

using $E(\kappa'_{1,\text{res}}) = E(\kappa'_{2,\text{res}})$ together with Eq. (21), we get

$$d_1 = \frac{\pi \hbar}{\sqrt{2(V_1 - V_2)}} \sqrt{\frac{1}{\alpha^2} \frac{n_2^2}{m_2} - \frac{n_1^2}{m_1}}. \quad (24)$$

In this way, given the materials 1 and 2 parameters, by choosing the integers n_1 and n_2 and a value for α such that $n_2^2/(n_1^2 \alpha^2) > m_2/m_1$, a FP resonance is obtained provided the two semiconductor layers of the CBB have widths d_1 and αd_1 , with d_1 satisfying Eq. (24).

To illustrate the above, consider InAlAs/InGaAs/X heterostructures, with $X = \text{GaAsSb}$ or $X = \text{InP}$, Fig. 11(b). The due material parameters are depicted in Table I. In Fig. 12 we show the transmission probabilities for: the whole heterostructures (with $N = 10$ cells or BBs), the single CBBs and the corresponding individual InAlAs and X barriers. In all instances $n_1 = 1$, $n_2/\alpha = 1.5$ and $\ell = L = (d_1 + d_2)/2$, with d_1 observing Eq. (24). As it should be, we always have a full transmission both for the heterostructures and the CBBs at an energy corresponding to the n_1 th and n_2 th transmis-

sion resonances of the InAlAs and X barriers. Another fairly general trend is that the transmission probability for a single CBB tends more closely to accompanying that for the highest barrier, in the present case the InAlAs (with $V_1 - V_0 = 520$ meV, Table I). Nonetheless, the oscillations of $|T|^2$ versus E of the lower CBB barrier, X, somehow better comply with the overall quasibands profile of the finite lattice. This pinpoints the influence of these more “transparent” barriers to establish the heterostructure global transport properties (in particular, see the right panels in Fig. 12). We finally observe that in Fig. 12(a) there is a very narrow peak at $E \approx 0.074$ eV, corresponding to a quasistate resonance of the CBB. As usual, this kind of resonance is relatively off the individual barriers FP modes.

VI. FINAL REMARKS AND CONCLUSION

In the present work, we have proposed a novel protocol to study quantum scattering in finite 1D periodic lattices formed by N equally spaced cells (or building blocks, BB). For so, one assumes that the $R(k)$ and $T(k)$ amplitudes of the BB forming the finite (but arbitrarily large) structure are known either analytically or numerically. The key idea is then to calculate the system Green’s function G explicitly from the underlying multiple scattering processes. From such a G , one can obtain the reflections R_N and transmission T_N coefficients of the full array written in terms of recurrence relations. Perhaps a bit surprising, these relations can be solved exactly in a closed analytic form by means of continued fractions methods.

As examples of BBs, we have assumed the simple but extremely common in applications delta, triangular, rectangular and trapezoidal barriers, whose R ’s and T ’s can be

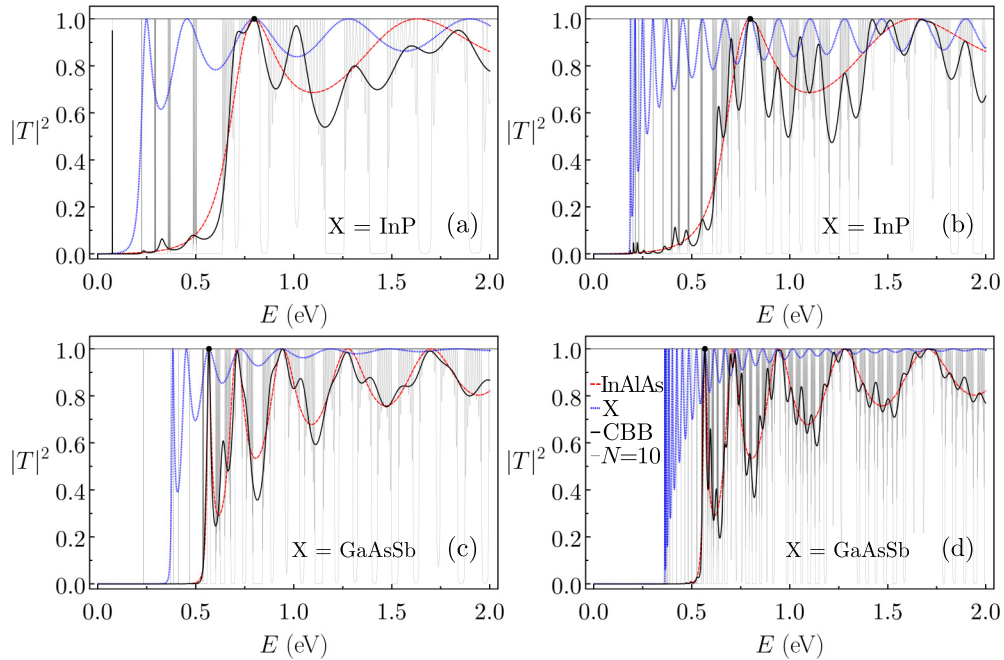


FIG. 12. The transmission probabilities for the full heterostructure (with $N = 10$ CBBs), the single CBB, and the two individual barriers, InAlAs and X, forming the CBBs. Here $X = \text{InP}$ in (a) and (b) and $X = \text{GaAsSb}$ in (c) and (d). The parameters are $n_2 = 3$, $\alpha = 2$ and $d_1 = 2$ in (a) and (c) and $n_2 = 9$, $\alpha = 6$ and $d_2 = 6$ in (b) and (d). In all cases $n_1 = 1$. When $X = \text{InP}$ ($X = \text{GaAsSb}$), the resonance energies are $E(\kappa'_{1,\text{res}}) = E(\kappa'_{2,\text{res}}) \approx 0.80$ eV ($E(\kappa'_{1,\text{res}}) = E(\kappa'_{2,\text{res}}) \approx 0.57$ eV). These values are indicated by a black dot in the graphs.

determined exactly. Nonetheless, we should remark that if for any localized $V(x)$ taken as a BB one can determine $R(k)$ and $T(k)$, say numerically, from any particular technique, one could combine this with our present scheme to solve long arrays of such $V(x)$'s. For the aforementioned four essential shapes, we have discussed distinct properties of lattices with N ranging from 10^6 to 10^9 , as far as we know sizes previously not addressed in the literature. In particular, for so large N 's the profiles of $|T_N(k)|^2$ are basically those of the energy bands of the corresponding infinite cases.

Furthermore, we have applied our method to arbitrary situations where the localized cells are themselves compositions of two or more basic BBs, generating which we have called CBBs. We have analyzed different CBBs, including spatially asymmetric ones. For them, our results helped to shed extra light into the comprehension of certain aspects of band structures of lattices constituted by asymmetric barriers. We remark that the unveiled general features here have previously been explored in specific instances, e.g., in Refs. [74,75].

Lastly, we have considered two concrete problems, namely, to search for spatial parameters optimizing the transport properties in heterostructures and to determine FP resonant modes in superlattices. The first (second) system has interest in the building of solar cells (band-pass filters). For so, we have addressed specific materials commonly discussed in the literature with such purposes. We have shown that our approach allows to easily test a broad range of parameters and situations through straightforward simulations, e.g., refer to Figs. 10(b) and 12. In particular, for the first problem our results have very adequately fitted the experimental results obtained in Ref. [13], Fig. 10(c).

We conclude this work by mentioning few possible extensions for our framework. An important effect in electron transmission through semiconductor superlattices is the so-called Rashba's, or, in brief, a spin-induced splitting of the energy bands (refer, e.g., to Refs. [91–93]). It is usually investigated for small arrays. Appropriate adaptations in our main equations to include the effect (presently an ongoing work) would allow us to consider much larger structures. For large lattices with the same basic BB, periodic replacement of BB by another BB', say after every M repetitions of BB, could give rise to distinct phenomena such as those related to conductance and transmittance in multi-junction solar cells [13], graphene layers [10,94], conjugated polymers [95,96], and organic semiconductors [97]. Ours is a very appropriate tool to calculate the properties of such types of systems. We finally observe that the TM is the common computation method to address processes in acoustics [98–102], optics [23,103], nanophotonics [104], organic thin films [105], many-body systems [106], and even in the microbiology, characterizing bacteria [107]. A great fraction of such works does consider only relatively small N 's. All these instances could likewise be treated with the present approach, however, permitting us to handle considerably greater N 's.

ACKNOWLEDGMENTS

This study was financed in part by the project ‘‘Efficiency in uptake, production and distribution of photovoltaic energy distribution as well as other sources of renewable en-

ergy sources’’ (Grant No. 88881.311780/2018-00) via CAPES PRINT-UFPR. L.R.N.O. acknowledges CAPES for a Ph.D. scholarship (Grant No. 8887.927924/2023-00). M.G.E. Luz acknowledges CNPq-Brazil for the research Grant No. 304 532/2019-3.

APPENDIX A: DEDUCTION OF THE EXPRESSION FOR C_N

Suppose two infinite sets of complex numbers b_0, b_1, \dots and $a_1, a_2, \dots \neq 0$. From the continued fractions theory [54,55], for

$$f = b_0 + \frac{a_1}{b_1 + \frac{a_2}{b_2 + \frac{a_3}{\ddots}}}, \quad (\text{A1})$$

one defines the n -th approximant of f as ($n = 1, 2, \dots$)

$$f_n = b_0 + \frac{a_1}{b_1 + \frac{a_2}{b_2 + \frac{a_3}{\ddots b_{n-1} + \frac{a_n}{b_n}}}}. \quad (\text{A2})$$

For instance, $f_1 = b_0 + a_1/b_1$, $f_2 = b_0 + a_1/(b_1 + a_2/b_2)$ and so on. Then, there is a sequence of complex numbers $\{X_n\}$ and $\{Y_n\}$ satisfying

$$\begin{aligned} X_n &= b_n X_{n-1} + a_n X_{n-2}, \\ Y_n &= b_n Y_{n-1} + a_n Y_{n-2}, \end{aligned} \quad (\text{A3})$$

such that for each n , it reads (exactly) $f_n = X_n/Y_n$. Above, $X_{-1} = 1$, $X_0 = b_0$, $Y_{-1} = 0$ and $Y_0 = 1$. The quantities X_n and Y_n are called, respectively, the n -th *numerator* and *denominator* of the associated continued fraction [54,108].

Now, for our C_N in Eq. (10), we have that $b_N = C_0$, $b_0 = b_1 = \dots = b_{N-1} = \gamma$ and $a_n = 1$ for any n . In this way, $C_N = X_N/Y_N$, where

$$\begin{aligned} X_N &= C_0 X_{N-1} + X_{N-2}, \\ Y_N &= C_0 Y_{N-1} + Y_{N-2}, \end{aligned} \quad (\text{A4})$$

and for any $n \leq N - 1$

$$\begin{aligned} X_n &= \gamma X_{n-1} + X_{n-2}, \\ Y_n &= \gamma Y_{n-1} + Y_{n-2}. \end{aligned} \quad (\text{A5})$$

The above equations are easily solved through recurrence methods, see, e.g., Refs. [109,110]. Indeed, both relations in Eq. (A5) are associated to the *characteristic equation* $\Gamma^2 - \gamma \Gamma - 1 = 0$, whose roots are

$$\Gamma_{\pm} = \frac{\gamma \pm \sqrt{\gamma^2 + 4}}{2}. \quad (\text{A6})$$

Thus, the solutions for Eq. (A5) are [109,110]

$$X_n = c_+ \Gamma_+^n + c_- \Gamma_-^n, \quad Y_n = \tilde{c}_+ \Gamma_+^n + \tilde{c}_- \Gamma_-^n, \quad (\text{A7})$$

where the constants c_{\pm} and \tilde{c}_{\pm} obey

$$\begin{aligned} \gamma &= c_+ + c_-, & 1 &= \tilde{c}_+ + \tilde{c}_-, \\ 1 &= c_+/\Gamma_+ + c_-/\Gamma_-, & 0 &= \tilde{c}_+/\Gamma_+ + \tilde{c}_-/\Gamma_-, \end{aligned} \quad (\text{A8})$$

resulting in

$$c_{\pm} = \pm \frac{\Gamma_{\pm}^2}{\sqrt{\gamma^2 + 4}}, \quad \tilde{c}_{\pm} = \pm \frac{\Gamma_{\pm}}{\sqrt{\gamma^2 + 4}}. \quad (\text{A9})$$

Finally, using Eqs. (A7) and (A9) in Eq. (A4), we get

$$C_N = \frac{C_0 [\Gamma_+^{N+1} - \Gamma_-^{N+1}] + [\Gamma_+^N - \Gamma_-^N]}{C_0 [\Gamma_+^N - \Gamma_-^N] + [\Gamma_+^{N-1} - \Gamma_-^{N-1}]}, \quad (\text{A10})$$

which after some simplifications yields Eq. (11).

APPENDIX B: DERIVATION OF THE SCATTERING AMPLITUDES FOR A TRAPEZOIDAL POTENTIAL

The trapezoid barrier is well discussed in the literature, with their exact reflection and transmission amplitudes used in many distinct contexts (see main text). However, it is very hard to find a comprehensive derivation of the corresponding R_{trap} and T_{trap} . So, our aim here is to fulfill such gap.

Thus suppose a 1D quantum particle of mass m subject to the localized potential

$$V(x) = \frac{(V_b - V_a)x + (V_a b - V_b a)}{(b - a)}, \quad a \leq x \leq b, \\ V(x) = 0, \quad \text{otherwise}, \quad (\text{B1})$$

notice that $V(a) = V_a$ and $V(b) = V_b$, see Fig. 3(c).

We have a free Schrödinger equation for $x < a$ and $x > b$, whereas for $a \leq x \leq b$, we get

$$\left(-\alpha^{-\frac{2}{3}} \frac{d^2}{dx^2} + \left(-x + \frac{(\tilde{\alpha} - k^2)}{\alpha} \right) \alpha^{\frac{1}{3}} \right) \psi(x) = 0, \quad (\text{B2})$$

for $\alpha = (2m/\hbar^2)(V_a - V_b)/(b - a)$, $\tilde{\alpha} = (2m/\hbar^2)(V_a b - V_b a)/(b - a)$ and $k^2 = (2mE)/\hbar^2$. Further, setting $y = [-x + (\tilde{\alpha} - k^2)/\alpha] \alpha^{1/3}$, it is easy to see that $d^2/dy^2 = \alpha^{-\frac{2}{3}} d^2/dx^2$, with Eq. (B2) reducing to

$$\left(-\frac{d^2}{dy^2} + y \right) \psi(y) = 0. \quad (\text{B3})$$

The above is the Airy equation, such that in the y interval corresponding to $a \leq x \leq b$

$$\psi(y) = \mathcal{A} \text{Ai}(y) + \mathcal{B} \text{Bi}(y), \quad (\text{B4})$$

with $\text{Ai}(y)$ and $\text{Bi}(y)$ the Airy functions of first and second kind, respectively [111].

For the cases of an incoming wave either from the left (+) or from the right (-), we write ($c^{(+)} = a$, $c^{(-)} = b$)

$$\psi(x) = \begin{cases} \exp[\pm i k x] + r^{(\pm)} \exp[\mp i k x], & x \leq c^{(\pm)} \\ \mathcal{A}^{(\pm)} \text{Ai}(y(x)) + \mathcal{B}^{(\pm)} \text{Bi}(y(x)), & a < x < b, \\ t^{(\pm)} \exp[\pm i k x], & x \geq c^{(\mp)} \end{cases} \quad (\text{B5})$$

subjected to the continuity of ψ and of $d\psi/dx$ at $x = a$ and $x = b$. Therefore (with $f'(z) = df(x)/dx|_{x=z}$ and $y_z = y(x = z)$)

$$0 = \mathcal{A}^{(\pm)} \text{Ai}(y_{c^{(\pm)}}) + \mathcal{B}^{(\pm)} \text{Bi}(y_{c^{(\pm)}}) - \exp[\pm i k c^{(\pm)}] - r^{(\pm)} \exp[\mp i k c^{(\pm)}], \\ 0 = \mathcal{A}^{(\pm)} \text{Ai}(y_{c^{(\mp)}}) + \mathcal{B}^{(\pm)} \text{Bi}(y_{c^{(\mp)}}) - t^{(\pm)} \exp[\pm i k c^{(\mp)}], \\ 0 = (\mathcal{A}^{(\pm)} \text{Ai}'(y_{c^{(\pm)}}) + \mathcal{B}^{(\pm)} \text{Bi}'(y_{c^{(\pm)}})) \alpha^{\frac{1}{3}} \pm i k (\exp[\pm i k c^{(\pm)}] - r^{(\pm)} \exp[\mp i k c^{(\pm)}]), \\ 0 = (\mathcal{A}^{(\pm)} \text{Ai}'(y_{c^{(\mp)}}) + \mathcal{B}^{(\pm)} \text{Bi}'(y_{c^{(\mp)}})) \alpha^{\frac{1}{3}} \pm i k t^{(\pm)} \exp[\pm i k c^{(\mp)}]. \quad (\text{B6})$$

Solving such a system, we obtain

$$R^{(\pm)}(k) = \frac{\mathcal{D}^{(\pm)}(k)}{\mathcal{C}(k)}, \quad T(k) = -\frac{2\eta(k)}{\pi \mathcal{C}(k)}, \quad (\text{B7})$$

with $\eta(k) = i \alpha^{\frac{1}{3}}/k$

$$\mathcal{D}^{(\pm)}(k) = [\text{Ai}(y_a) \mp \eta(k) \text{Ai}'(y_a)] [\text{Bi}(y_b) \mp \eta(k) \text{Bi}'(y_b)] - [\text{Ai}(y_b) \mp \eta(k) \text{Ai}'(y_b)] [\text{Bi}(y_a) \mp \eta(k) \text{Bi}'(y_a)], \\ \mathcal{C}(k) = [\text{Ai}(y_a) + \eta(k) \text{Ai}'(y_a)] [\text{Bi}(y_b) - \eta(k) \text{Bi}'(y_b)] - [\text{Ai}(y_b) - \eta(k) \text{Ai}'(y_b)] [\text{Bi}(y_a) + \eta(k) \text{Bi}'(y_a)]. \quad (\text{B8})$$

Recall that $r^{(\pm)}(k) = \exp[\pm 2 i k c^{(\pm)}] R^{(\pm)}(k)$ and that $t^{(\pm)}(k) = \exp[-i k (b - a)] T^{(\pm)}(k)$.

APPENDIX C: FEW COMPARISONS WITH THE LITERATURE

We shall recall that our method is exact. In this way, there is no need to confront ours with other calculations in the literature, at least for accuracy. Nonetheless, few checks would be in order. So, we mention that in different papers, e.g., Refs. [19–21,112–115], distinct methods have been used to obtain $|T_N|^2$ for arrays formed by equally spaced delta

functions, considering N never superior to one hundred. Although not explicitly shown here (but see below), as it should be we have been able to exactly and extremely rapid reproduce the $|T_N|^2$ plots of all these works. Likewise, we have easily generated the same $|T_N|^2$ of Refs. [19,28,31,116,117] for periodic systems composed by few rectangular barriers. Unfortunately, we have not found studies of finite 1D lattices whose BBs are either trapezoidal or triangular potentials.

However, for explicit comparisons, in Fig. 13, we confront ours (indicated as Green Function, GF) with the results from two pioneers works of 1992 and 1993 [19,20], in which the transfer matrix (TM) method was employed for $N = 100$

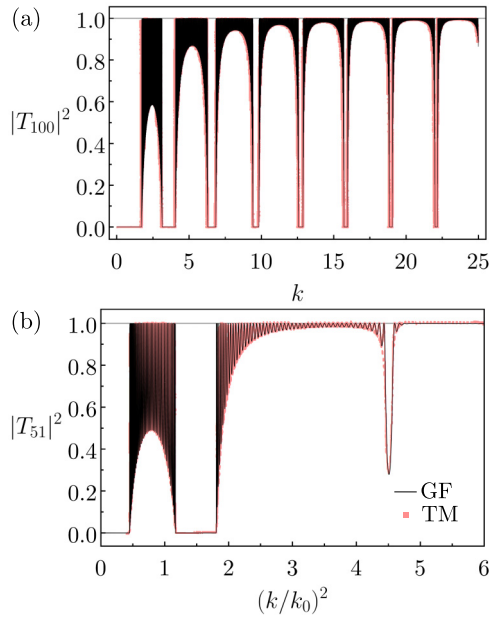


FIG. 13. Transmission probability as a function of (a) k for $N = 100$ delta barriers with $\beta = 4$, $L = 1$ and of (b) $(k/k_0)^2$ for $N = 51$ rectangular barriers with $V_0 = 2$, $w = L = \pi/8$ ($k_0^2 = V_0$). The calculations from TM—digitalized from Refs. [19,20], respectively, in (a) and (b)—are compared with the present method, here labeled as GF (Green’s function method).

deltas and $N = 51$ rectangular barriers. The curves in Fig. 13 for the TM have been electronic digitalized directly from such references, whose original print quality has not the present-day resolution. Nevertheless, taken this into account, one sees that our approach reproduces perfectly well these previous computations. Finally, in Fig. 14, we present $|T_{10}|^2$ curves for systems with ten attractive delta potentials ($\beta < 0$) [113]—solved by means of the Lippmann–Schwinger (LS) equation—and ten rectangular barriers [117], calculated from the TM method. Our method is indicated as GF. We again observe fully agreement between the curves. Also important to mention that in Fig. 14(a), we have delta wells instead of barriers. This illustrates that our protocol is not restricted to repulsive potentials.

APPENDIX D: THE FORBIDDEN BANDS ONSETS: THE CASE OF AN ARBITRARY LONG DIRAC COMB

Here we determine analytically the onsets of forbidden (quasi)bands in a Dirac comb of arbitrary N . Although this result has already been derived in the literature (see, e.g., Refs. [19,21]), our current Green’s function approach makes it easier to grasp why such onsets are the same regardless of N .

If for a given k the periodic structure is transparent, or $|T_N(k)|^2 = 1$ (so $|R_N(k)|^2 = 0$), the Eq. (14) implies that $C_N/C_0 = 1$. Conversely, if there is no transmission through the lattice for a certain k , i.e., $|T_N(k)|^2 = 0$ (so $|R_N(k)|^2 = 1$), the Eq. (14) implies that $C_N/C_{N-1} = 1$. In particular, for a forbidden band starting at k_* , we should have $T_N(k_* + \varepsilon) = 0$ for $0 \leq \varepsilon < \Delta k$, with Δk the bandwidth.

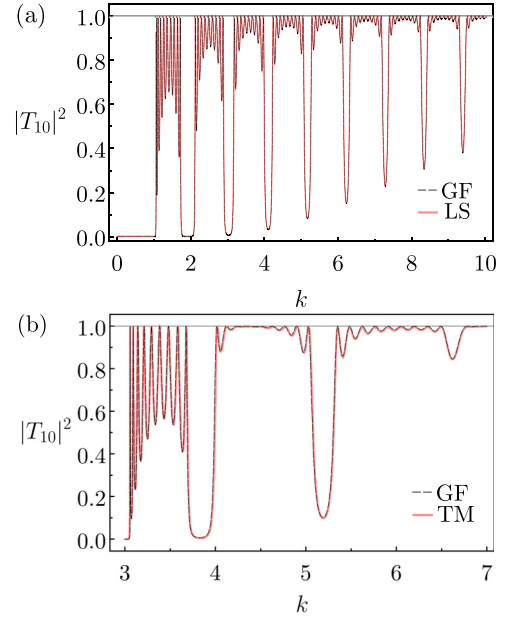


FIG. 14. Transmission probability versus k for finite structures formed by $N = 10$ (a) delta wells, with $\beta = -2$, $L = 3$ and (b) rectangular barriers, with $V_0 = 18$, $w = L = 1$. The results from the present exact approach (GF) are compared with those from the Lippmann–Schwinger (LS) equation [113] (for the deltas) and from the transfer matrix (TM) method [117] (for the rectangular barriers). The curves from LS and TM have been digitalized from the corresponding references [113,117].

Moreover, $\lim_{\varepsilon \rightarrow 0^+} |T_N(k_* - \varepsilon)| > 0$ (but regarding this requirement there are some subtleties, see below).

By defining

$$A = \frac{(1 + C_0 \Gamma_-)}{(1 + C_0 \Gamma_+)} = B \Delta, \quad B = \frac{(C_0 - \Gamma_+)}{(C_0 - \Gamma_-)}, \quad (\text{D1})$$

from the Eq. (11), we can write

$$\begin{aligned} \frac{C_N}{C_{N-1}} &= \frac{(A \Delta^N - 1)(B \Delta^N - \Delta)}{(A \Delta^N - \Delta)(B \Delta^N - 1)} \\ &= 1 - \frac{B \Delta^N}{\Delta} \left(\frac{\Delta - 1}{B \Delta^N - 1} \right)^2. \end{aligned} \quad (\text{D2})$$

Note that for any \bar{k} such that $\Delta(\bar{k}) = 1$ —or equivalently $\gamma(\bar{k})^2 + 4 = 0$, refer to Eq. (12)—from Eq. (D2) we find that $C_N(\bar{k})/C_{N-1}(\bar{k}) = 1$ and thus $T_N(\bar{k}) = 0$. However, to determine whether or not $\bar{k} = k_*$, we must perform the aforementioned analyzes, i.e., to study T_N around \bar{k} .

Thus suppose N equally spaced delta potentials. For R_δ and T_δ in Eq. (18) (for which $\phi = 0$) and γ in Eq. (8), one has $\gamma(k) = -2i(\cos[kL] + \beta \sin[kL]/(2k))$. Thence, for $kL = l\pi$ ($l = 1, 2, \dots$) it readily follows $\gamma(l\pi)^2 + 4 = 0$. Next, considering $kL = l\pi + \varepsilon$ with ε very small, in first order in ε we get

$$\gamma \approx -2i(-1)^l \left(1 + \frac{\beta L}{2l\pi} \varepsilon \right). \quad (\text{D3})$$

Also, for Γ_{\pm} and Δ in Eq. (12) and C_0 as defined in Sec. III B, in first order in ε

$$\begin{aligned} \Gamma_{\pm} &\approx -i(-1)^l \left(1 + \frac{\beta L}{2l\pi} \varepsilon \right) \pm i \sqrt{\frac{\beta L}{l\pi}} \varepsilon, \\ \Delta &\approx 1 + \frac{2\beta L}{l\pi} \varepsilon + 2(-1)^l \sqrt{\frac{\beta L}{l\pi}} \varepsilon, \\ C_0 &\approx -i(-1)^l \left\{ \left(1 + i \frac{\beta L}{2l\pi} \right) - i \left(1 + i \frac{\beta L}{2l\pi} \right) \varepsilon \right. \\ &\quad \left. - i \frac{\beta L}{2l\pi} \frac{1}{l\pi} \varepsilon \right\}. \end{aligned} \quad (D4)$$

To infer the behavior of T_N just to the left and just to the right of $kL = l\pi$, we can take only the terms up to $\sqrt{\varepsilon}$ in Eq. (D4) and split the analysis into two case: ε either positive or negative.

Writing $\Delta = 1 + \xi$ for $\xi = 2(-1)^l \sqrt{\frac{\beta L}{l\pi}} \varepsilon$ — so $|\xi|$ is small—we have $A \approx (1 + \xi)B$, $C_N/C_{N-1} \approx 1 - D_N$ and

$$D_N = \frac{B}{(1 + \xi)^{N+1}} \frac{\xi^2}{(B - (1 + \xi)^{-N})^2}. \quad (D5)$$

We also set $B \approx 1 - 2i(l\pi/(\beta L))\xi$. Further simplifications for D_N depends on the small ξ being real or imaginary (ε positive or negative). Indeed, for ξ real obviously $1/(1 + \xi)^M$ is likewise real (with M any integer) and a fairly good approximation is $1/(1 + \xi)^M \approx 1 - M\xi$. But if ξ is imaginary, $1/(1 + \xi)^M$ is a complex number. Therefore a more suitable approximation is $1/(1 + \xi)^M \approx \exp[-iM|\xi|] = \cos[M|\xi|] - i \sin[M|\xi|]$.

For the former situation

$$D_N \approx \frac{1 - (N + 1 + i2l\pi/(\beta L))\xi}{(N - i2l\pi/(\beta L))^2}, \quad (D6)$$

so that D_N is rather small for $N \geq |\xi|^{-1}$, yielding $|T_N(l\pi + |\varepsilon|)^2 \approx 0$. On the other hand, for the latter

$$D_N \approx -\frac{B \exp[-i(N + 1)|\xi|]}{(B - \exp[-iN|\xi|])^2} |\xi|^2. \quad (D7)$$

Due to the oscillatory character of $\exp[-iN|\xi|]$, D_N can vary, assuming smaller or larger values depending on N and ε . Consequently, this is also true for $|T_N(l\pi - |\varepsilon|)^2$, a well known phenomenon within the allowed quasibands in a periodic array as one increases the number N of its barriers [19].

In this way, we can conclude that $k_* = l\pi$ is in fact the onset of the forbidden bands in the Dirac comb model.

[1] R. G. Newton, *Scattering Theory of Waves and Particles* (Springer Science and Business Media, Berlin, 2013).

[2] L. Brillouin, *Wave Propagation in Periodic Structures* (Dover Publications, Mineola, 2003).

[3] A. Bensoussan, J. L. Lions, and G. Papanicolaou, *Asymptotic Analysis for Periodic Structures* (American Mathematical Society, Ann Arbor, 2011).

[4] D. G. Truhlar and B. Simon, *Multiparticle Quantum Scattering with Applications to Nuclear, Atomic and Molecular Physics* (Springer Science and Business Media, New York, 1997).

[5] B. J. Berne and R. Pecora, *Dynamic Light Scattering: With Applications to Chemistry, Biology, and Physics* (Dover Publications, Mineola, 2000).

[6] D. Colton and R. Kress, *Inverse Acoustic and Electromagnetic Scattering Theory* (Springer Berlin, Heidelberg, 2019).

[7] P. A. Martin, *Time-Domain Scattering* (Cambridge University Press, Cambridge, 2021).

[8] Z. Cao and C. Yin, *Advances in One-Dimensional Wave Mechanics: Towards a Unified Classical View* (Springer Berlin, Heidelberg, 2014).

[9] E. Sakr, A. El-Nadi, and I. Eshrah, *Spatial Modulation of One-Dimensional Periodic Structures: Analysis and Applications* (LAP LAMBERT Academic Publishing, Saarbrücken, 2012).

[10] L. G. Wang and S. Y. Zhu, Electronic band gaps and transport properties in graphene superlattices with one-dimensional periodic potentials of square barriers, *Phys. Rev. B* **81**, 205444 (2010).

[11] X. Fang, Y. Bando, U. K. Gautam, T. Zhai, S. Gradečak, and D. Golberg, Heterostructures and superlattices in one-dimensional nanoscale semiconductors, *J. Mater. Chem.* **19**, 5683 (2009).

[12] A. T. Tilke, F. C. Simmel, H. Lorenz, R. H. Blick, and J. P. Kotthaus, Quantum interference in a one-dimensional silicon nanowire, *Phys. Rev. B* **68**, 075311 (2003).

[13] A. Gonzalo *et al.*, Strain-balanced type-II superlattices for efficient multi-junction solar cells, *Sci. Rep.* **7**, 4012 (2017).

[14] P. Pereyra, *Fundamentals of Quantum Physics: Textbook for Students of Science and Engineering* (Springer Berlin, Heidelberg, 2012).

[15] P. A. Kalozoumis, G. Theocharis, V. Achilleos, S. Félix, O. Richoux, and V. Pagneux, Finite-size effects on topological interface states in one-dimensional scattering systems, *Phys. Rev. A* **98**, 023838 (2018).

[16] G. Buchs, D. Bercioux, P. Ruffieux, P. Gröning, H. Grabert, and O. Gröning, Electron scattering in intranantotube quantum dots, *Phys. Rev. Lett.* **102**, 245505 (2009).

[17] E. Glushkov, N. Glushkova, A. Eremin, and R. Lammering, Trapped modes and resonance wave transmission in a plate with a system of notches, *J. Sound Vib.* **412**, 360 (2018).

[18] O. Richoux, V. Tournat, and T. LeVanSuu, Acoustic wave dispersion in a one-dimensional lattice of nonlinear resonant scatterers, *Phys. Rev. E* **75**, 026615 (2007).

[19] D. W. L. Sprung, H. Wu, and J. Martorell, Scattering by a finite periodic potential, *Am. J. Phys.* **61**, 1118 (1993).

[20] D. J. Griffiths and N. F. Taussig, Scattering from a locally periodic potential, *Am. J. Phys.* **60**, 883 (1992).

[21] D. Kiang, Multiple scattering by a Dirac comb, *Am. J. Phys.* **42**, 785 (1974).

[22] P. Pereyra, The transfer matrix method and the theory of finite periodic systems: From heterostructures to superlattices, *Physica Status Solidi (b)* **259**, 2100405 (2022).

- [23] T. G. Mackay and A. Lakhtakia, *The Transfer-Matrix Method in Electromagnetics and Optics* (Springer Nature, Berlin, 2022).
- [24] A. Dell, A. Krynkin, and K. V. Horoshenkov, The use of the transfer matrix method to predict the effective fluid properties of acoustical systems, *Appl. Acoust.* **182**, 108259 (2021).
- [25] C. Jirauschek, Accuracy of transfer matrix approaches for solving the effective mass Schrödinger equation, *IEEE J. Quantum Electron.* **45**, 1059 (2009).
- [26] R. Pérez-Álvarez, R. Pernas-Salomón, and V. R. Velasco, Relations between transfer matrices and numerical stability analysis to avoid the Ωd problem, *SIAM J. Appl. Math.* **75**, 1403 (2015).
- [27] M. Feyzollahzadeh and M. Bamdad, A modified transfer matrix method to reduce the calculation time: A case study on beam vibration, *Appl. Math. Comput.* **378**, 125238 (2020).
- [28] M. Hasan and B. P. Mandal, Super periodic potential, *Ann. Phys.* **391**, 240 (2018).
- [29] X. Luo, J. Shi, Y. Zhang, Z. Niu, D. Miao, H. Mi, and W. Huang, Filtering electrons by mode coupling in finite semiconductor superlattices, *Sci. Rep.* **12**, 7502 (2022).
- [30] S. Das, Exact solution for one dimensional multibarrier tunneling, [arXiv:1310.8234](https://arxiv.org/abs/1310.8234).
- [31] S. Das, Tunneling through one-dimensional piecewise-constant potential barriers, *Am. J. Phys.* **83**, 590 (2015).
- [32] L. J. Boya, Quantum-mechanical scattering in one dimension, *Riv. Nuovo Cim.* **31**, 75 (2008).
- [33] F. Gesztesy, Scattering theory for one-dimensional systems with nontrivial spatial asymptotics, in *Lecture Notes in Mathematics*, edited by E. Balslev (Springer, Berlin, 2006).
- [34] A. Boutet de Monvel, I. Egorova, and G. Teschl, Inverse scattering theory for one-dimensional Schrödinger operators with steplike finite-gap potentials, *J. Anal. Math.* **106**, 271 (2008).
- [35] I. Egorovaab, Z. Gladkaa, T. L. Langeb, and G. Teschlbc, Inverse scattering theory for Schrödinger operators with steplike potentials, *J. Mat. Phys. Anal. Geom.* **11**, 123 (2015).
- [36] J. Horáček and T. Sasakawa, Method of continued fractions with application to atomic physics, *Phys. Rev. A* **28**, 2151 (1983).
- [37] J. Horáček and T. Sasakawa, Method of continued fractions with application to atomic physics II, *Phys. Rev. A* **30**, 2274 (1984).
- [38] J. Horáček and T. Sasakawa, Method of continued fractions for on-and off-shell T matrix of local and nonlocal potentials, *Phys. Rev. C* **32**, 70 (1985).
- [39] M.-T. Lee, I. Iga, M. M. Fujimoto, and O. Lara, The method of continued fractions for electron (positron)-atom scattering, *J. Phys. B* **28**, L299 (1995).
- [40] M.-T. Lee, I. Iga, M. M. Fujimoto, and O. Lara, Application of the method of continued fractions for electron scattering by linear molecules, *J. Phys. B* **28**, 3325 (1995).
- [41] M.-T. Lee, M. M. Fujimoto, and I. Iga, Application of the method of continued fractions to low-energy electron scattering by the hydrogen molecule, *J. Mol. Struct.* **394**, 117 (1997).
- [42] J. P. Vigneron and P. Lambin, Transmission coefficient for one-dimensional potential barriers using continued fractions, *J. Phys. A* **13**, 1135 (1980).
- [43] P. Lambin and J. P. Vigneron, Improved continued fraction treatment of the one-dimensional scattering problem, *J. Phys. A* **14**, 1815 (1981).
- [44] H. Mori, A continued-fraction representation of the time-correlation functions, *Prog. Theor. Phys.* **34**, 399 (1965).
- [45] M. M. Evans, P. Grigolini, and G. P. Parravicini, *Memory Function Approaches to Stochastic Problems in Condensed Matter* (John Wiley and Sons, New York, 2009).
- [46] J. J. Bissell and A. M. Nagaitis, Infinity, self-similarity, and continued fractions in physics: Applications to resistor network puzzles, *Phys. Educ.* **57**, 055014 (2022).
- [47] A. Wierling, Fitting the dielectric response of collisionless plasmas by continued fractions, *Phys. Plasmas* **16**, 112105 (2009).
- [48] K. Hattori, T. Hattori, and H. Watanabe, Block spin approach to the singularity properties of the continued fractions, *Commun. Math. Phys.* **115**, 31 (1988).
- [49] M. G. E. da Luz, E. J. Heller, and B. K. Cheng, Exact form of Green's functions for segmented potentials, *J. Phys. A* **31**, 2975 (1998).
- [50] M. G. E. da Luz, B. K. Cheng, and M. W. Beims, Asymptotic Green functions: A generalized semiclassical approach for scattering by multiple barrier potentials, *J. Phys. A* **34**, 5041 (2001).
- [51] A. G. M. Schmidt, B. K. Cheng, and M. G. E. da Luz, Green's functions for generalized point interactions in one dimension: A scattering approach, *Phys. Rev. A* **66**, 062712 (2002).
- [52] F. M. Andrade, B. K. Cheng, M. W. Beims, and M. G. E. da Luz, A generalized semiclassical expression for the eigenvalues of multiple well potentials, *J. Phys. A* **36**, 227 (2003).
- [53] F. M. Andrade, A. Schmidt, E. Vicentini, B. Cheng, and M. G. E. da Luz, Green's function approach for quantum graphs: An overview, *Phys. Rep.* **647**, 1 (2016).
- [54] W. B. Jones and W. J. Thron, *Continued fractions: Analytic Theory and Applications* (Addison-Wesley Publishing Company, Massachusetts, 1980).
- [55] O. N. Karpenkov, *Geometric Continued Fractions* (Springer Berlin, Heidelberg, 2022).
- [56] N. W. Ashcroft and N. D. Mermin, *Solid State Physics* (Saunders College Publishing, New York, 1976).
- [57] A. Raja *et al.*, Coulomb engineering of the bandgap and excitons in two-dimensional materials, *Nat. Commun.* **8**, 15251 (2017).
- [58] C. Li, Exact analytical solution of the ground-state hydrogenic problem with soft Coulomb potential, *J. Phys. Chem. A* **125**, 5146 (2021).
- [59] W. Li, Z. Yang, M. Sun, J. Dong, Interlayer interactions in transition metal dichalcogenides heterostructures, *Rev. Phys.* **9**, 100077 (2022).
- [60] H. Iwamoto, V. M. Aquino, and V. C. Aguilera-Navarro, Scattering coefficients for a trapezoidal potential, *Int. J. Theor. Phys.* **42**, 1795 (2003).
- [61] Q. Luo, Y. Jiang, L. Shen, W. Xu, and J. Han, Calculation of the transmission coefficient for one-dimensional trapezoid potential barrier, *Coll. Phys.* **33**, 42 (2014).
- [62] S. Albeverio, F. Gesztesy, R. Hoegh-Krohn, and H. Holden, *Solvable Models in Quantum Mechanics* (Springer-Verlag, New York, 1988).

- [63] B. M. Sutherland, *Beautiful Models: 70 Years of Exactly Solved Quantum Many-Body Problems* (World Scientific Publishing, Singapore, 2004).
- [64] I. Reshodko, A. Benseny, J. Romhányi, and T. Busch, Topological states in the Kronig–Penney model with arbitrary scattering potentials, *New J. Phys.* **21**, 013010 (2019).
- [65] N. L. Harshman and P. Singh, Entanglement mechanisms in one-dimensional potential scattering, *J. Phys. A* **41**, 155304 (2008).
- [66] R. Ghosh and A. Das, Disorder-induced enhancement of entanglement growth in one dimension: Information leakage at the scale of the localization length, *Phys. Rev. B* **103**, 024202 (2021).
- [67] F. Marsiglio and R. L. Pavelich, The tight-binding formulation of the Kronig–Penney model, *Sci. Rep.* **7**, 17041 (2017).
- [68] S. E. Ulloa, E. Castao, and G. Kirczenow, Ballistic transport in a novel one-dimensional superlattice, *Phys. Rev. B* **41**, 12350 (1990).
- [69] T. E. Hartman and J. S. Chivian, Electron tunneling through thin aluminum oxide films, *Phys. Rev.* **134**, A1094 (1964).
- [70] A. Schenk and G. Heiser, Modeling and simulation of tunneling through ultra-thin gate dielectrics, *J. Appl. Phys.* **81**, 7900 (1997).
- [71] L. Wei-Yi, R. Guo-Ping, J. Yu-Long, and R. Gang, Trapezoid mesa trench metal-oxide semiconductor barrier Schottky rectifier: An improved Schottky rectifier with better reverse characteristics, *Chin. Phys. B* **20**, 087304 (2011).
- [72] M. Dessai and A. V. Kulkarni, Calculation of tunneling current across trapezoidal potential barrier in a scanning tunneling microscope, *J. Appl. Phys.* **132**, 244901 (2022).
- [73] F. Ambriz-Vargas, G. Kolhatkar, M. Broyer, A. Hadj-Youssef, R. Nouar, A. Sarkissian, R. Thomas, C. Gomez-Yáñez, M. A. Gauthier, and A. Ruediger, A complementary metal oxide semiconductor process-compatible ferroelectric tunnel junction, *ACS Appl. Mater. Interfaces* **9**, 13262 (2017).
- [74] C. M. Hurd, Asymmetric scattering of electrons in metals, *Contemp. Phys.* **16**, 517 (1975).
- [75] A. Ruschhaupt, T. Dowdall, M. A. Simón, and J. G. Muga, Asymmetric scattering by non-Hermitian potentials, *Europhys. Lett.* **120**, 20001 (2017).
- [76] M. Ohmukai, Triangular double barrier resonant tunneling, *Mater. Sci. Eng. B* **116**, 87 (2005).
- [77] F. Nutku, Quasi-bound levels, transmission and resonant tunneling in heterostructures with double and multi rectangular, trapezoidal, triangular barriers, *J. Comput. Electron.* **13**, 456 (2014).
- [78] B. de A. Mello, I. F. da Costa, C. R. Lima, and L. Cescato, Developed profile of holographically exposed photoresist gratings, *Appl. Opt.* **34**, 597 (1995).
- [79] M. Yamaguchi, F. Dimroth, J. F. Geisz, and N. J. Ekins-Daukes, Multi-junction solar cells paving the way for super high-efficiency, *J. Appl. Phys.* **129**, 240901 (2021).
- [80] M. Gibert-Roca, M. Casademont-Viñas, Q. Liu, K. Vandewal, A. R. Goñi, and M. Campoy-Quiles, RAINBOW organic solar cells: Implementing spectral splitting in lateral multi-junction architectures, *Adv. Mater.* **36**, 2212226 (2024).
- [81] U. Aeberhard, A. Gonzalo, and J. M. Ulloa, Photocarrier extraction in GaAsSb/GaAsN type-II QW superlattice solar cells, *Appl. Phys. Lett.* **112**, 213904 (2018).
- [82] K. I. Lin, K. L. Lin, B. W. Wang, H. H. Lin, and J. S. Hwang, Double-band anticrossing in GaAsSbN induced by nitrogen and antimony incorporation, *Appl. Phys. Express* **6**, 121202 (2013).
- [83] K. Sakamoto and H. Yaguchi, First-principles study on the conduction band electron states of GaAsN alloys, *Phys. Status Solidi C* **11**, 911 (2014).
- [84] H.-H. Tung and C.-P. Lee, An energy band-pass filter using superlattice structures, *IEEE J. Sel. Top. Quantum Electron.* **32**, 507 (1996).
- [85] G. V. Morozov, D. W. L. Sprung, and J. Martorell, Design of electron band-pass filters for semiconductor superlattices, *J. Phys. D Appl. Phys.* **35**, 3052 (2002).
- [86] J. Martorell, D. W. L. Sprung, and G. V. Morozov, Design of electron band pass filters for electrically biased finite superlattices, *Phys. Rev. B* **69**, 115309 (2004).
- [87] S. Mukherjee and B. Muralidharan, Electronic Fabry-Perot cavity engineered nanoscale thermoelectric generators, *Phys. Rev. Appl.* **12**, 024038 (2019).
- [88] D. Prete *et al.*, Thermoelectric conversion at 30 K in InAs/InP nanowire quantum dots, *Nano Lett.* **19**, 3033 (2019).
- [89] H. Karbaschi, J. Lovén, K. Courteau, A. Wacker, and M. Leijnse, Nonlinear thermoelectric efficiency of superlattice-structured nanowires, *Phys. Rev. B* **94**, 115414 (2016).
- [90] X. Luo, H. Zhang, D. Liu, N. Han, D. Mei, J. Xu, Y. Cheng, and W. Huang, Efficiency at maximum power of thermoelectric heat engines with the symmetric semiconductor superlattice, *Physica E* **129**, 114657 (2021).
- [91] M. C. Araujo, A. F. Silva, and E. A. de Andradae Silva, Electron spin-orbit split minibands in semiconductor asymmetric superlattices, *Phys. Rev. B* **65**, 235305 (2002).
- [92] E. A. de Andradae Silva, G. C. La Rocca, and F. Bassani, Spin-orbit splitting of electronic states in semiconductor asymmetric quantum wells, *Phys. Rev. B* **55**, 16293 (1997).
- [93] E. A. de Andradae Silva and G. C. La Rocca, Electron-spin polarization by resonant tunneling, *Phys. Rev. B* **59**, R15583 (1999).
- [94] T. Zhan, X. Shi, Y. Dai, X. Liu, and J. Zi, Transfer matrix method for optics in graphene layers, *J. Phys.: Condens. Matter* **25**, 215301 (2013).
- [95] J. Hwang, D. B. Tanner, I. Schwendeman, and J. R. Reynolds, Optical properties of nondegenerate ground-state polymers: Three dioxothiophene-based conjugated polymers, *Phys. Rev. B* **67**, 115205 (2003).
- [96] Z. Peng, Y. Zhang, Y. Xia, K. Xiong, C. Cai, L. Xia, Z. Hu, K. Zhang, F. Huang, and L. Hou, One-step coating inverted polymer solar cells using a conjugated polymer as an electron extraction additive, *J. Mater. Chem. A* **3**, 20500 (2015).
- [97] C. Kaiser, S. Zeiske, P. Meredith, and A. Armin, Determining ultralow absorption coefficients of organic semiconductors from the sub-bandgap photovoltaic external quantum efficiency, *Adv. Opt. Mater.* **8**, 1901542 (2020).
- [98] J. H. Han, Y. J. Kim, and M. Karkoub, Modeling of wave propagation in drill strings using vibration transfer matrix methods, *J. Acoust. Soc. Am.* **134**, 1920 (2013).
- [99] K. Verdière, R. Panneton, S. Elkoun, T. Dupont, and P. Leclaire, Transfer matrix method applied to the parallel assembly of sound absorbing materials, *J. Acoust. Soc. Am.* **134**, 4648 (2013).

- [100] O. Doutres, N. Atalla, and H. Osman, Transfer matrix modeling and experimental validation of cellular porous material with resonant inclusions, *J. Acoust. Soc. Am.* **137**, 3502 (2015).
- [101] D. H. Lee and Y. P. Kwon, Estimation of the absorption performance of multiple layer perforated panel systems by transfer matrix method, *J. Sound Vib.* **278**, 847 (2004).
- [102] G. Campa and S. M. Camporeale, in *Proceedings of the European COMSOL Conference, Paris, 2010* (COMSOL, Inc., Paris, 2010).
- [103] A. Menéndez-Manjón, P. Wagener, and S. Barcikowski, Transfer-matrix method for efficient ablation by pulsed laser ablation and nanoparticle generation in liquids, *J. Phys. Chem. C* **115**, 5108 (2011).
- [104] R. B. Balili, Transfer matrix method in nanophotonics, *Int. J. Mod. Phys. Conf. Ser.* **17**, 159 (2012).
- [105] L. A. A. Pettersson, L. S. Roman, and O. Inganäs, Modeling photocurrent action spectra of photovoltaic devices based on organic thin films, *J. Appl. Phys.* **86**, 487 (1999).
- [106] X. Rui, X. Wang, Q. Zhou, and J. Zhang, Transfer matrix method for multibody systems (Rui method) and its applications, *Sci. China Technol. Sci.* **62**, 712 (2019).
- [107] A. N. Nilsson, G. Emilsson, L. K. Nyberg, C. Noble, L. S. Stadler, J. Fritzsche, E. R. B. Moore, J. O. Tegenfeldt, T. Ambjörnsson, and F. Westerlund, Competitive binding-based optical DNA mapping for fast identification of bacteria-multi-ligand transfer matrix theory and experimental applications on *Escherichia coli*, *Nucleic Acids Res.* **42**, e118 (2014).
- [108] D. Hensley, *Continued Fractions* (World Scientific, Singapore, 2006).
- [109] K. A. Ross and C. R. Wright, *Discrete Mathematics* (Prentice-Hall, Inc., Upper Saddle River, 2003).
- [110] H. S. Wilf, *Generatingfunctionology* (CRC press, Boca Raton, 2005).
- [111] M. Abramowitz and I. A. Stegun, *Handbook of Mathematical Functions with Formulas, Graphs, and Mathematical Tables* (US Government printing office, Washington D. C., 1970).
- [112] K. Rapadius and H. J. Korsch, Multi-barrier resonant tunnelling for the one-dimensional nonlinear Schrödinger Equation, *J. Phys. A* **42**, 425301 (2009).
- [113] F. Erman, M. Gadella, and H. Uncu, On scattering from the one-dimensional multiple Dirac delta potentials, *Eur. J. Phys.* **39**, 035403 (2018).
- [114] P. Berman, Transmission resonances and Bloch states for a periodic array of delta function potentials, *Am. J. Phys.* **81**, 190 (2013).
- [115] M. Dharani and C. S. Shastri, Band structures in transmission coefficients generated by Dirac comb potentials, *Phys. B: Condens. Matter* **500**, 66 (2016).
- [116] H. Yamamoto, Y. Kanie, M. Arakawa, and K. Taniguchi, Theoretical study of resonant tunneling in rectangular double-, triple-, quadruple-, and quintuple-barrier structures, *Appl. Phys. A* **50**, 577 (1990).
- [117] P. Erdős, E. Livio, and R. C. Herndon, Wave transmission through lattices, superlattices and layered media, *J. Phys. D* **30**, 338 (1997).